The Pennsylvania State University

The Graduate School

MECHANICS OF CELL-SUBSTRATE INTERACTION

A Dissertation in

Engineering Science and Mechanics

by
Tiankai Zhao

Submitted in Partial Fulfillment
of the Requirements
for the degree of

Doctor of Philosophy

August 2020

The dissertation of Tiankai Zhao was reviewed and approved by the following:

Sulin Zhang
Professor of Engineering Science and Mechanics
Dissertation Advisor
Chair of Committee

Long-Qing Chen
Hammer Professor of Material Science and Engineering
Professor of Engineering Science and Mechanics
Professor of Mathematics

Christian Peco Regales
Assistant Professor of Engineering Sciences and Mechanics

Spencer Szczesny
Assistant Professor of Biomedical Engineering

Judith A. Todd
Department head of ESM
P. B. Breneman Chair
Professor of Engineering Science and Mechanics

ABSTRACT

Mechanics of cell-substrate interactions has recently emerged one of the most exciting topics to study, propelled by the discovery of unusual fundamental physical phenomena such as durotaxis and newly developed experimental techniques such as Traction-force-microscopy (TFM). The intensive interest on the mechanics of cell-substrate interactions arises also because of the decisive role that forces play in well-known biological processes such as proliferation, durotaxis, and metastasis. The discovery of the novel importance of cell-substrate interactions has inspired an endeavor that leads to the establishment of new physical theories. Such monumental pushes, however, still have some flaws based on the assumptions and simplifications and require a deeper physical understanding and more detailed modeling on the mechanism of cell-substrate interactions.

This dissertation contributes to the mechanics of cell-substrate interactions and mainly focuses on the establishment of physical models based on formulating the free energy of cell-substrate interactions. As a living cell adheres to a substrate, it will contract, pull the substrate, and generate external tensions. The Rho and Ca pathways control the stress-dependent myosin motor recruitment and binding with the cytoskeleton. The stress fiber network applies tensile forces on the ligand-receptor complex, which facilitates the aggregation of the complex and forms the focal adhesions. The focal adhesions then transmit more tensions between the cell and the substrate, enabling more and more myosin motor activation and stress fiber assembly. This positive feedback loop is the mechanism of cell-substrate interaction.

Enormous efforts have been undertaken in computationally modeling cell-substrate interactions. Formal models proposed on cell-substrate interactions are either too simplified which fail to capture the essential details or too complicated which are difficult to implement. To achieve both physical accuracy and computational efficiency, this dissertation aims to develop new models to predict the focal adhesion formation, the traction force generation, and the stress fiber assembly in cell-substrate interactions. In particular, the free energy is written as a functional of the cellular displacement, the integrin density and myosin motor density. The equilibrium is achieved by finding the minimum of the functional. For the time-dependent evolution of stress fiber assembly, a phase-field method is applied to trace the morphology of stress fibers at any given time. To deal with the irregular shapes of cells, the finite element method is used to solve the equations. A commercial package named COMSOL is used as the major computing tool in this dissertation.

The new models enable the prediction of the traction forces, the formation of focal adhesions and stress fibers; and they replicate a range of interesting phenomena observed in experiment, typically inaccessible to previous models and experiments. For arbitrary-shaped single cells on homogeneous substrate, our model is able to predict the profile of the traction force and the focal adhesion, which are determined by the geometry of the cells. We find that the intracellular tension is highly dependent on the shape of the patterned cell on glass and governs the number of the nanoparticle uptake. For strip-like cells on alternatively coated gels, our model suggests that the interfacial tension play an important role in a variety of interesting phenomena such as dorsal stress fiber bending and dorsal stress fiber formation failure. For cohesive cell colonies, a variety of experimental observations, such as the size effect and the stiffness effect, are replicated by our

model. We also conclude that the metastasis is governed by the intercellular tension from the model. These findings show not only the effectiveness of the new model, but also the possible guidance that the model can offer to the further study on cell-substrate interactions.

TABLE OF CONTENTS

LIST OF FIGURES viii

LIST OF TABLES xiv

ACKNOWLEDGEMENTS xv

Chapter 1 Introduction 1

1.1 Background 1
1.2 Motivation 5
1.3 Outline 9

Chapter 2 A thermodynamic model for cellular force generation and transmission of single cells and multicellular structures 11

2.1 Introduction 11
2.2 Equations 12
2.3 Numerical implementation 19
2.4 Conclusion and summary 23

Chapter 3 Applications of the thermodynamic model to single cells and cohesive monolayers 24

3.1 Introduction 24
3.2 Cellular contractility depends on substrate stiffness 25
3.3 Geometry regulated traction force landscape and focal adhesion distribution for single cells 27
3.4 Geometry regulated nanoparticle uptake of patterned cells on glass 29
3.5 Active, nonlinear cell-matrix coupling of HCT-8 colonies 33
3.6 Intracellular traction and intercellular tension are both gel stiffness and colony size dependent 37
3.7 Cellular-force threshold exists at pre-dispersion stage for the dispersion behavior 40
3.8 Conclusion and summary 43

Chapter 4 Phase-field model for the prediction of the distribution of myosin motors and the morphology of the stress fibers 44

4.1 Introduction 44
4.2 Equations 46
4.3 Numerical implementation 49
4.4 Results and applications 52
4.5 Conclusion and summary 69

Chapter 5 Conclusion 70

Appendix A Model parameters used in the dissertation 72

Appendix B Supplementary figures to determine the phase diagram on actin node formation 76

References 78

LIST OF FIGURES

Figure 2.1. Schematics of cellular force generation mediated by focal adhesion formation through integrin clustering. (a) Randomly distributed, freely diffusive integrins (red dots) on the cell membrane. (b) Focal adhesion formation through integrin clustering upon cell-substrate interactions. (c) The molecular structure of the focal adhesion. 12

Figure 2.2. Schematics of force generation mediated by focal adhesion formation through integrin clustering in a multicellular monolayer. (a) Randomly distributed, freely diffusive integrins (red dots) on cell membrane. (b) Focal adhesion formation through integrin clustering upon cell-substrate interactions. (c) Molecular structure of the focal adhesions. 17

Figure 3.1. Average substrate traction stress, as measured experimentally (black squares) and predicted active stress by data matching (magenta triangles), versus substrate shear elastic modulus. Error bars represent standard error of the mean. Experimental data are from [21]. The model parameters are listed in Table. A.1 in Appendix A. 25

Figure 3.2. Substrate stiffness mediates cell contractility. Active stress versus Young's modulus of substrate $\hat{E}$ obtained by experimental-numerical matching of the traction forces. The model parameters are listed in Table. A.2 in Appendix A. 26

Figure 3.3. Traction force is regulated by the cellular geometry. Column A: Phase contrast images of SaOS-2 cells on different gel Young's modulus (from top to bottom: 4kPa, 10kPa and 20kPa, respectively; scale bar: 30μm). Column B1~B2: The traction force profiles of the cells obtained from experiments and modeling, respectively. The model parameters are listed in Table. A.1 in Appendix A. 28

Figure 3.4. Focal adhesion (represented as the stained FAK) and stress fiber distribution. (a) Stained stress fiber and FAK. (b) Stained FAK. (c) Predicted first principal stress by color contour and its direction by arrow. Red means large and blue means small. Stress fiber directions align with the maximum principle stress, marked by the semi-transparent circles.

(d) Predicted focal adhesion distribution. Red means the higher density and blue means lower density. 29

Figure 3.5. Top row: focal adhesion distribution versus different aspect ratios predicted by our thermodynamic model; bottom row: focal adhesion distribution versus different aspect ratios by experiment. The model parameters are listed in Table A.1 in Appendix A. 31

Figure 3.6. Predictions made by the thermodynamic model. Top row: internal stress profile versus different aspect ratios; middle row: traction force landscape versus different aspect ratios; bottom row: focal adhesion distribution versus different aspect ratios. 32

Figure 3.7. The decay of the magnitude of displacement from the periphery to the centroid of HCT-8 colony of 186μm in radius, predicted by the models, normalized by the maximum value. 34

Figure 3.8. Nonlinear reciprocal cell-matrix coupling. Left: (a) Immunofluorescence staining shows localization of focal adhesion kinase (FAK) at the boundary layer of a monolayer. (b) The traction force map measured by TFM. (c)-(d) The traction force maps predicted by the previous uniform coupling model (c, constant Y) and the current nonlinear coupling model (d, nonlinear Y) model, subtracted by the map from TFM in (b). The darker the pixel, the better the agreement of the traction force. (e) The decay of the radial component of traction force from the periphery to the centroid of HCT-8 colony of 186 μm in radius, shown in (b), predicted by the models and TFM. All the results are normalized by the maximum average radial traction forces. 35

Figure 3.9. The distribution of coupling strength from the periphery to the centroid of HCT-8 colony of 186μm in radius, predicted by the models, normalized by the maximum value. 37

Figure 3.10. Traction force is both substrate stiffness (Left panel) and colony size (Right panel) dependent. (a1-a2): Phase contrast images of HCT-8 cell colonies on different gel stiffness (a1,with gel stiffness of 4.5kPa, 20.7kPa and 47.1kPa, respectively; scale bar: 90μm) and with

different monolayer sizes (a2, scale bar: 45μm) on 20.7kPa gels. (b-c) The traction force profiles of the cell colonies obtained by TFM (b1-b2) and modeling (c1-c2), respectively. (d-e) The intercellular tension maps of the cell colonies obtained by MSM (d1-d2) and modeling (e1-e2). The model parameters are listed in Table. A.2 in Appendix A. 39

Figure 3.11. Traction force is both substrate stiffness (Left panel) and colony size (Right panel) dependent. (a-b): Phase contrast images of HCT-8 cell colonies on different gel stiffness (a1,with gel stiffness of 4.5kPa, 20.7kPa and 47.1kPa, respectively; scale bar: 100μm) and with different monolayer sizes (a2, scale bar: 100μm) on 20.7kPa gels. (c-f) The traction force profiles of the cell colonies obtained by TFM (c-d) and modeling (e-f), respectively. (g-j) The intercellular tension maps of the cell colonies obtained by MSM (g-h) and modeling (i-j). (k) Spatial distribution of traction force (solid line) and intercellular tension (dash line), normalized by their maxima, respectively. (l) The average traction force at the boundary layer (the summation of traction force in the region within 50 mm from colony boundary divided by the area of the region). 41

Figure 3.12. Phase diagram of average traction at the boundary layer in the stiffness-size plane computed by the biophysical model, overlapped with the dispersion behavior of many cell colonies observed in the experiments. The dashed lines represent constant traction contours in the parametric space. A phase boundary of constant traction 125Pa, separating the dispersive and cohesive cell colonies, is identified, representing a force-threshold criterion for the malignant phenotypic change. 42

Figure 4.1. Experimental and simulation results of a single needle-like 3T3 fibroblast: upper left: phase contrast of the cell; upper right: TFM results of the cell; bottom left: the concentration profile of the myosin motors in the cell; bottom right: the predicted traction force landscape. 52

Figure 4.2. Validation of the size and stiffness effect by the new model. (a) Traction force landscapes of cohesive colonies with radius 60μm, 100μm, and 150μm on 20kPa gel. (b)Traction force landscapes of colonies with a 150μm radius on substrates with Young's modulus of 6kPa, 20kPa, and 40kPa. (c)Left: average traction force in boundary layer

versus colony radius on 20kPa gels; right: average traction force in boundary layer versus gel Young's modulus for colonies with the same radius..... 54

Figure 4.3. Our model captures cadherin-dependent organization of traction stresses. (a) Schematic of planar colony of three cells, the cell-cell junctions are modeled as a series of linear springs. (b) The traction force landscape versus different cell-cell junction strength. (c) Spatial profiles of average strain traction force as a function of distance, from colony edge for different cell-cell junction strength. 56

Figure 4.4. The knot-like stress fiber formation in strip-shape cells patterned on substate with heterogeneous surface. (a) The surface of the substrate is alternatively coated with fibronectin in rectangular blocks (the blue part), while the gap has no fibronectin coated. (b) Stained actins show inhomogeneity of actin node formation and stress fiber assembly in a patterned cell. Actin nodes form in the non-adhesive patches of the cell and vanish in the non-adhesive patches of the cell..... 57

Figure 4.5. he illustration of the interfaces after the gel surface is partially coated with fibronectin. Here three surface tension: Γ_{cf}, Γ_{cg}, and Γ_{gf} form the Neumann triangle. 58

Figure 4.6. Physical process happened in the cell on alternatively coated substrate. The purple arrows on the top and bottom boundaries of the non-adhesive patch denote for the effective line force $\Delta\Gamma$ led by the difference in the interfacial tensions. The purple arrows on the left and right boundaries of the non-adhesive patch denote for the effective pulling force led by the line tension. Red arrows stand for the traction forces. 60

Figure 4.7. Morphology of stress fibers with respect to different gap size on 10.6kPa gel. (a) Experimental results on stress fiber formation. Pictures have been taken with respect to different gap size. Actin fiber is extracted from the pictures for each case and plotted aside. (b) Simulation of stress fiber formation denoted by the first principal stress σ_1. Colors stand

for magnitude of σ_1 and arrows stand for the direction. Red means large and blue means small.....61

Figure 4.8. The simulation results on the first principal stress (a) and myosin motor density (b) and focal adhesion concentration (c) with respect to different gap sizes. Red means large and blue means small..... 62

Figure 4.9. Cells with 4μm gap size on gels with different stiffness. (a)Experimental results on stress fiber configuration 2.8kPa, 7.4kPa, 10.6kPa, 16.7kPa, and 34.9kPa gels, ands glass (b) Predicted stress fiber direction, denoted by the direction of the first principal stress σ_1, are shown by arrow, whose length is proportional to the average of σ_1.The color contour map represents the magnitude of σ_1..... 64

Figure 4.10. Cells with 10μm gap size on gels with different stiffness. (a)Experimental results on stress fiber configuration 2.8kPa gel, 10.6kPa gels, ands glass (b) Predicted stress fiber direction, denoted by the direction of the first principal stress σ_1, are shown by arrow, whose length is proportional to the average of σ_1.The color contour map represents the magnitude of σ_1. 65

Figure 4.11. The stress fiber configuration of cells with 6μm, 8μm 10μm gap size on gels with different stiffness. (a) 2.8kPa gel; (b) 7.4kPa gel; (c) 10.6kPa gel; (d) 16.7kPa gel; (e) glass. The predicted stress fiber direction is denoted by the direction of the first principal stress σ_1, are shown by arrow, whose length is proportional to the average of σ_1.The color contour map represents the magnitude of σ_1, which is used to represent the stress fiber density. 67

Figure 4.12. The phase diagram on actin node formation. The horizontal axis is for the gap size, while the perpendicular axis is for the gel stiffness. In the green region, actin node is formed, yet in the blue region, actin node formation fails. 68

Figure B.1. The phase diagram on $\bar{\sigma}$, overlapped with the action node formation of cells observed in the experiments. The horizontal axis is for the gap size, while the perpendicular axis

is for the gel stiffness. A phase boundary of $\bar{\sigma} = \sigma_c = 70\text{Pa}$ is identified by the white dashed line. The symbol "◯" stands for the success of actin node formation, while "×" stands for the failure of actin node formation. 76

Figure B.2. The phase diagram on $\bar{n}$, overlapped with the action node formation of cells observed in the experiments. The horizontal axis is for the gap size, while the perpendicular axis is for the gel stiffness. Two phase boundaries of $\bar{n} = n_c^u = 0.7$, and $\bar{n} = n_c^l = 0.3$, are identified by the black dashed lines. The symbol "◯" stands for the success of actin node formation, while "×" stands for the failure of actin node formation. 76

Figure B.3. The phase diagram on Δn, overlapped with the action node formation of cells observed in the experiments. The horizontal axis is for the gap size, while the perpendicular axis is for the gel stiffness. The phase boundary of $\Delta n = \Delta n_c = 0.14$ is identified by the black dashed line. The symbol "◯" stands for the success of actin node formation, while "×" stands for the failure of actin node formation. 77

LIST OF TABLES

Table 2.1. The average internal stress in the whole cell vs. aspect ratio. 32

Table 2.2. The average internal stress in the central region of the cell (occupies the 1/4 of the total area) vs. aspect ratio. 33

Table A.1. Model parameter used for single SaOs-2 cells and patterned NIH 3T3 cells in Chapter 2 and 3. 72

Table A.2. Model parameter used for HCT-8 cohesive colonies in Chapter 2 and 3. 73

Table A.3. Model parameter used for the validation part of Section 4.4. 73

Table A.4. Model parameter used for patterned strip-shape cells. 74

.

ACKNOWLEDGEMENTS

I am indebted to my advisor, Dr. Sulin Zhang, for his constant encouragement, patient guidance throughout my Ph.D. study. This dissertation would not be finished without his support and advice. The knowledge and experience gained through discussions with him are priceless.

I thank my other committee members, Dr. Longing Chen, Dr. Christian Peco Regales, and Dr. Spencer Szczesny for their advice and guidance.

I thank my fellow lab mates, Yao Zhang, Qiong Wei, Peng Zhao, Tianwu Chen, and Xuechen Shi, for their support and constructive discussions.

I thank the Department of Engineering Science and Mechanics and the College of Engineering at Penn State for the financial assistance.

I would like to specially thank my families for their unconditional support and love. They are my biggest motivation to go through ups and downs.

Chapter 1

Introduction

1.1. Background

Cellular mechanotransduction

It is well-known that cells can interact with substrate through the process called mechanotransduction in which mechanical stimuli is translated into biochemical signals, enabling cells to adapt to the substrate it adheres on [1]. A variety of behaviors in cell-substrate interactions, such as adhesion, migration, growth, proliferation, and cancer metastasis, are mediated by the mechanotransduction [2-5], which is critical for multicellular tissues to maintain integrity and homeostasis. Enormous efforts have been devoted to study cellular mechanotransduction. It is clear that adherent cells must attach to a substrate for survival and growth. Once they attach to the substrate, they establish contractility and homeostasis by either pulling the substrate to generate extracellular traction forces, or by pulling neighboring cells to generate intercellular forces. Both forces will then be transmitted into cells to generate intracellular tensions to help cells stay in a uniform tension state. The cellular contractility is generated by the activation of myosin motors. Myosin motors are usually free diffusive inside cells and can aggregate and bind to stress fibers when they feel the stress-activated signaling molecules. They pull the stress fibers and stress fibers assemble into the cytoskeletons which are

the main structures inside cells to sustain intracellular forces. The force transmission between cells and substrates mainly relies on cell-substrate adhesions which include four types based on the size, the shape, and the location [6, 7]. Although there are distinct differences among them, these structures undergo dynamic changes and can evolve from one type to another [6]. Amongst those four, focal adhesions (FAs) are the largest ones and hence are the main structure that transmit forces from substrate to cells. They are mainly consisted of dynamic protein complexes, such as the integrin-ligand complexes, which connect the extracellular matrix to the cytoskeleton. Integrin, a transmembrane receptor binding with both the substrate and cellular actin filaments via adapter proteins, is considered as the major mechanosensors among proteins in focal adhesions (including integrins, talin, paxillin and signaling molecules such as focal adhesion kinase). Focal adhesions are bridges that enable the transmission of mechanical forces and regulatory signals between the substrate and the cell. Its formation and maturation can be modulated and promoted by external mechanical forces [8, 9]. Cell-cell adhesions, like cell-matrix adhesions, are in responsible for signal transmission between neighboring cells, and also play an important role in cell-substrate interactions. They are categorized into adherent junctions, tight junctions, and gap junctions; and are mediated by cadherins, occludins, and connexins, respectively [10-11]. The cadherin-mediated adherent junction is the one responsible for transmitting mechanical signals among the three since they are directly connected to the actin filaments. They too can affect the cell-substrate interactions.

Traction force microscopy

The traction forces are the forces that a cell exerts onto the substrate. Traction forces quantify the intensity of cell-substrate interactions. As traction forces modulate many biological processes

such as formation of FAs, migration, differentiation, metastasis and angiogenesis, the measurements of traction forces have drawn intensive research interest in the biomechanical field. A methodology called the traction force microscopy (TFM) has been developed to measure the traction force [12-13]. Different from the traction force, the intercellular and intracellular forces within multicellular structures are difficult to be directly measured but can be calculated from the traction force map by performing force equilibrium. In this case, these forces are characterized by stress tensors.

The principle of TFM is quite straightforward and simple. Firstly, one need to deliver fluorescent beads into the substrate with a proper depth: neither too deep nor too shallow to be devoured by cells. Then one could culture cells on substrate. Cells will deform the substrate, and so will the beads displace. At this time one can take a picture of the current position of the beads and then wash away the cells. The beads return to their original positions and another picture can be taken now. By comparing the different location of the beads in the two pictures, one is able to find the displacement of the beads, i.e., the displacement of the substrate at those particular locations. Reconstructing the force field from the displacement field is solving an inverse elasticity problem. For substrate, whose thickness is much larger than the displacement caused by the cell traction force, it can be considered as an elastic half-space medium bounded by an infinite plane. The analytic solution of displacements on the free surface due to the point forces has been derived by L. D. Landan and E. M. Lifshitz [14]. It is known as Boussinesq solution given by the convolution between green's function and point forces:

$$u_i(x,y) = \iint G_{ij}(x-x', y-y')\, f_j(x',y') dx'y', \qquad (1\text{-}1)$$

where subscript i, j take the values 1 and 2, u_i (x, y) is the i-th component of displacement at the point (x,y), $f_j(x',y')$ is the j-th component of point force at the point (x',y'), and $G_{ij}(x-x',y-y')$ is the green's function. The green's function is expressed as:

$$G(x-x', y-y') = \frac{1+\nu}{\pi E r^3}\begin{bmatrix}(1-\nu)r^2 + \nu r_x^2 & \nu r_x r_y \\ \nu r_x r_y & (1-\nu)r^2 + \nu r_y^2\end{bmatrix}, \tag{1-2}$$

Where $r_x = x - x'$, $r_y = y - y'$, $r = \sqrt{r_x^2 + r_y^2}$, ν is Poisson's ratio of the elastic substrate and E is its Young's modulus. The complex convolution equation (1-1) can be converted into a simple multiplication by Fourier transform (FT). In the Fourier space, the equation (1-1) can be written as:

$$\tilde{u}_{ik} = \{\tilde{G}_{ij}\tilde{f}_k\}_k, \tag{1-3}$$

Where k is the mode in the frequency domain, $\tilde{\mathbf{u}}$ is the displacement in the Fourier space, $\tilde{\mathbf{G}}$ is the green's function in the Fourier space and $\tilde{\mathbf{f}}$ is the force in the Fourier space. The green's function in Fourier space is expressed as:

$$\tilde{G}_k = \frac{2(1+\nu)}{Ek^3}\begin{bmatrix}(1-\nu)k^2 + \nu k_y^2 & \nu k_x k_y \\ \nu k_x k_y & (1-\nu)k^2 + \nu k_x^2\end{bmatrix}, \tag{1-4}$$

Where k_x and k_y are the components of the wave vector k, $k = \sqrt{k_x^2 + k_y^2}$. Then the traction force in Fourier space would be:

$$\tilde{f}_{ik} = \{\tilde{G}_{ij}^{-1}\tilde{u}_j\}_k, \tag{1-5}$$

By applying the inverse Fourier transform on equation (1-5), one can get the traction forces in real space.

As the limitation of 2D TFM, it is assumed that the displacement perpendicular to substrate surface is zero. If the vertical component of traction force is notable and the resulting vertical displacement is not negligible, TFM does not work. That is because PIV analysis only enables the displacement measurement in one plane.

1.2. Motivation

Although TFM proves itself to be an effective method to get the traction forces in two-dimensional cell-substrate interactions, it still suffers from some flaws. Firstly, such experiments take a lot of time on preparing samples [15-17]. Researchers would spend a large amount of energy on carefully delivering the beads into a proper depth in gels. Secondly, since the accuracy of TFM mostly relies on the accuracy of the displacement one measures, if the substrate is very rigid, such as PDMS, the measured displacement will be so small that it loses quite a lot of accuracy [15-17]. Therefore, the situations require people to come up with a physical model which is easy to perform on computers to predict the traction force profiles by giving the geometry and the constitutive law of the cells. Enormous efforts have been made to develop models to simulate the cell-substrate interactions and try to predict the traction force landscape. A simple model is proposed by Mertz, A.F. *et al* at very first [18-20]. The model considers a cell as a thin elactic sheet and the focal adhsions as uniformly distributed linear springs. The stress equlibrium in the cell sheet is written as:

$$\nabla \cdot \boldsymbol{\sigma} - \frac{Y\mathbf{u}}{h} = \mathbf{0}, \tag{1-1}$$

where $\boldsymbol{\sigma}$ is the stress tensor in the cell; $\mathbf{u}$ is the displacemnet vector in the cell; Y is the effective stength of the focal adhesion and is assumed to be uniform on the whole cell sheet; h is the thickness of the cell sheet. The traction force equals to: $\mathbf{T} = Y\mathbf{u}$. The model successfully captures the deacy of the traction force from the priphery to the centroid in a circular cohesive cell colony. The model is then used to study a cell adhering on substrate with different thicknesses. Oakes, P.W. *et al* further introduces the line tension acting on cell boundaries and successfully replicates the traction profile of NIH 3T3 fibroblasts [21]. However, since the assumption of uniformly distibuted focal adhesion is used, the model fails to capture the external-force-mediated focal adhesion formation and hence loses the essential details in cell-substrate interactions. Besides, the contractility of cells on gels with different stiffness is assumed to be unchanged, which is also contradictory to experimental observtions. Another model proposed by Deshpande V.S. et al. has been looking into the great details in cell-substrate interactions [22-23]. The stress fiber in the cell is modeled as a piece of viscoelastic material whose constitutive law is a function of the activation level η of stress fibers. The constitutive law trise to capture the formation and dissociation of stress fibers, as well as the associated generation of tensions and contractilities. The variable η is defined as the ratio of the concentration of the polymerized actin and phosphorylated myosin within a stress fiber bundle to the maximum concentrations permitted by the biochemistry. The evolution of η is described by the following kinetic equation:

$$\dot{\eta} = (1-\eta)\frac{C\bar{k}_f}{\theta} - (1-\frac{\sigma}{\sigma_0})\eta\frac{\bar{k}_b}{\theta}, \tag{1-2}$$

where C is a biomechanical impulse that triggers the signaling cascade in the cell, which can be thought as the concentration of Ca^{+}. The parmamters θ, $\bar{k}_f$, $\bar{k}_b$ and σ_0 denote for the decay

constant, the rate of stress fiber association and dessociation, and the isometric stress, respectively. The tension inside the stress fiber is denoted by σ, which is:

$$\frac{\sigma}{\sigma_0} = \begin{cases} 0, & \frac{\dot{\varepsilon}}{\dot{\varepsilon}_0} < -\frac{\eta}{\bar{k}_v}, \\ 1 + \frac{\bar{k}_v}{\eta}\left(\frac{\dot{\varepsilon}}{\dot{\varepsilon}_0}\right), & -\frac{\eta}{\bar{k}_v} \leq \frac{\dot{\varepsilon}}{\dot{\varepsilon}_0} \leq 0, \\ 1, & \frac{\dot{\varepsilon}}{\dot{\varepsilon}_0} > 0. \end{cases} \quad (1\text{-}3)$$

where ε is the strain in the stress fiber; $\bar{k}_v$ and $\dot{\varepsilon}_0$ are the rate sensitivity coeffeicent and stress fiber shortening rate, respectively. The total active stress tensor is derived by summing the tensions in the stress fibers in all directions together. As we can see, this model looks into the great details of the physics in stress fibers. However, the kinetics in Equation (1-2) is not derived from a free energy functional, instead, it is derived phenologically. Moreover, the disribution of stress fibers with rescpect to diffrerent orientations needs to be measured at the very first stage. Therefore, their study is restricted to one-dimensinal cells and two-dimensional cells with very regular shapes. Instead of simulating the biomechanics in each single stress fiber, Shenoy V. et al. propose a chemo-mechanical free-energy-based approach to durotaxis and extracellular stiffness-dependent contraction and polarization of cells [24]. The one-dimesional-case free energy density $U(\rho, \varepsilon)$ of the cell consists of three parts: the mechanical energy in the cell (the first two terms),the chemical energy of myosin motors (the next two terms), and the motor-work (the last term):

$$U(\rho, \varepsilon) = \frac{K}{2}\varepsilon^2 - \int_0^{\varepsilon} \sigma \mathrm{d}\varepsilon + \frac{\beta}{2}(\rho - \rho_0)^2 - \alpha \int_0^{\rho} \sigma \mathrm{d}\rho + \rho\varepsilon, \quad (1\text{-}4)$$

where ρ, ε, and σ are the density of motors, the strain, and the stress,respectively. The motor density in the absence of stress is the quiescent value: ρ_0. The simple expression of the free energy can be easily extened to higher-dimesional cases and the constitutive law for the three-dimesional case is:

$$\sigma_{ij} = (\bar{\rho}_0 + \overline{K}\varepsilon_{kk})\delta_{ij} + 2\bar{\mu}\tilde{\varepsilon}_{ij}, \quad (1\text{-}5)$$

where ε_{kk} and $\tilde{\varepsilon}_{ij}$ are the volumetric part and deviatoric part of the strain, respectively. The parameter $\bar{\rho}_0$, $\overline{K}$, and $\bar{\mu}$ are the effective contractilty, the effective bulk modulus, and the effective shear modulus, respectively. Although this model is easy to apply and successfully predicts a few biomechanical phenomena, it still suffers from some flaws. For instance,the part of the chemical energy, especially the third term in Equation (1-4) does not strictly follow thernodynamic laws. Additionally, this model cannot predict the assembly and disassmbly of focal adhesions, instead, the model has to assume the focal adhesion distribution to simulate cell-substrate interactions. The review on the previous work motivtes us to develop new models that can capture the major biomechanics in cell-substrate interactions, such as tranction force generation and transmission, and myosin motor evolution without the models being too complicated.

In this dissertation, we propose two new models to study cell-substrate interactions, both derived from the free energies of the systems. In the first model, we mainly focus on the focal adhesion fomation as focal adhesions are the keys that determine the traction force profile. The cell membrane are categrized into three phases: a phase that the integrins are freely-diffusive, a phase that the integrins bind with ligands, and a vacancy phase. The three phases undergo dynamic changes and can evlove into one another. A free energy functional on the concentration of the different types of integrins is construted based on thermodynamics. The cell contractility is considered as a changing parameter versus subtrate stiffness. Edge effect is taken into account by considering the line energy on cell boundaries. We apply this model to circular NIH 3T3 fibroblasts to reveal the substrate stiffness depenedent contractility. We then apply the model to SaOS-2 cells on deformable substrate with irregular shapes to show the geometry regulated

traction forces. We also adopt this model to predict the traction force and focal adhesion distribution of cells patterned on glass and reveal the correlation between the intracellular tension and nanoparticle uptake to show the advantage of our model compared with TFM. Finally, we apply the model on multicellular structures and investigate the correlation between traction forces and metastasis. In the second model, we focus on the myosin motor evolution and stress fiber assembly. To fullfill this purpose, we introduce a new variable that characterizes the concentration of myosin motors. A new energy functional is then formulated. The new variable is modeled as a phase-field order parameter and the phase-field method is used to study the evolution of myosin motors. The density of the actin filaments and the directions of stress fibers are characterized by the magnitude and the direction of the first principal stress. We first use the model to replicate previous conclusions to validate its correctness. We then apply the model to predict the acting node formation in strip-shape cells adhereing on substrate with alternatively coated surface to reveal the vital role played by interfacial tensions in cell-substrat interactions. The simulation results not only advance the fundmental understandings on cell-substrate interactions, but also offer new pathways and tools in further study.

1.3. Outline

In this dissertation, two models have been proposed to study cell-substrate interactions and a varaity of cases have been investigated. In chapter 2, the first model is introduced, as well as the parameter settings. In chapter 3, we apply the model to single cells and cohesive colonies. We simulate the traction force profile, the focal adhesion distribution and the intracellular tension in single cells. For the cohesive colonies, the size effect and stiffness effect are discussed. The

traction force driven colony dispersion is also studied. In chapter 4, the second model is introduced. Knot-like stress fiber assembly is studied on alternatively coated substrate and the importance of interfacial tension is addressed. In chapter 5, we summarize our work and arrive at the conclusions.

. **Chapter 2**

A thermodynamic model for cellular force generation and transmission of single cells and multicellular structures

2.1. Introduction

As a basic unit of living lives, cells are able to consume nutrition from its surroundings and convert it into energy for their proliferation, migration, and other biological activities [25-27]. Unlike traditional materials, cells are alive. They can actively probe and sense physical cues from the surroundings and respond them by triggering a cascade of a series of biochemical signals [28, 29]. Usually, living cells attach to something in order to maintain the homeostasis. The cell-substrate interactions include both the chemical ones and mechanical ones and they are usually coupled. Among these interactions, the traction forces that a cell exerted on the substrate are of great importance and draw an intensive research interest from the biomechanical field [30-32]. It is found that the traction forces can mediate a lot of biological process such as cell migration, differentiation, and cancer metastasis [32]. Therefore, it is worth looking into the mechanism of the traction force generation and transmission of cells.

In this chapter, we develop a molecularly based thermodynamic model that simultaneously incorporates the elastic, edge, and interfacial effects in single cells. We formulate the free energy functional associated with the receptors. We also take strain energy in the cell and the substrate,

and the line energy on the cell boundary into account. The chemical equilibrium for receptors, the stress equilibrium for cells and substrates, along with the boundary conditions are derived by making the variations on the free energy functional. Next, we extend the thermodynamic model from single cells to multicellular structures. At last, we discuss the way to implement the model in COMSOL.

2.2. Equations

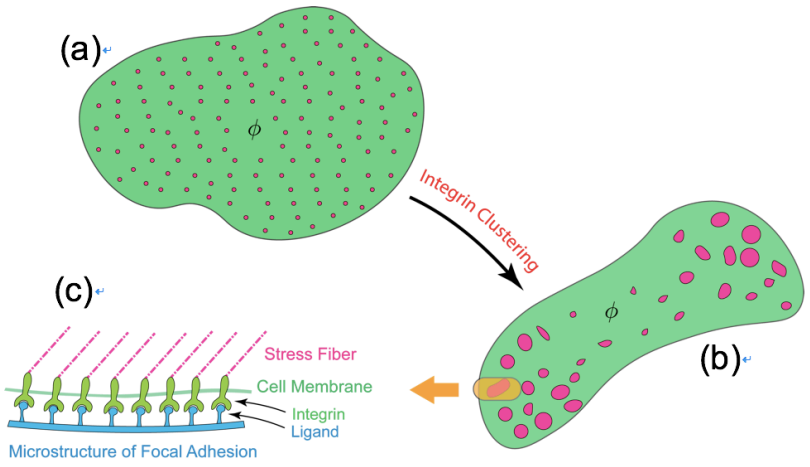

Fig. 2.1. Schematics of cellular force generation mediated by focal adhesion formation through integrin clustering. (a) Randomly distributed, freely diffusive integrins (red dots) on the cell membrane. (b) Focal adhesion formation through integrin clustering upon cell-substrate interactions. (c) The molecular structure of the focal adhesion.

Upon a contractile cell seeding on a hydrogel coated with fibronectins, the mechanosensory integrin receptors on the cell membrane probe the local mechanical cues and respond by emanating a series of outside-in biochemical signals. The signals activate the actomyosin motors to contract, and subsequently cause cytoskeletal remodeling, stress fiber formation, and cell spreading [33].

The contractile force is transmitted to the integrin receptors, resulting in integrin clustering [34-36] and focal adhesion maturation [37]. The focal adhesions, the cytoskeleton, and the cell contractile machinery thus form a structural network and a positive feedback loop that regulate cellular force generation and transmission [38, 39]. The focal adhesion points transmit mechanical forces between the cell and the hydrogel, causing both to elastically deform. The out-of-plane displacement is generally small compared to the in-plane displacement. We denote the 2D in-plane displacement fields of the cell and the hydrogel by $\mathbf{u}(\mathbf{x})$ and $\hat{\mathbf{u}}(\mathbf{x})$ at a point $\mathbf{x}$, respectively. Then $\Delta\mathbf{u} \equiv \hat{\mathbf{u}} - \mathbf{u}$ characterizes the relative displacement at the cell-substrate interface. In the case that a ligand-receptor pair exists at $\mathbf{x}$, $\Delta\mathbf{u}$ is the stretch in the ligand-receptor bond. A microstructure-based description is adopted here to simulate the formation of focal adhesion points through integrin clustering. The integrins on the cell membrane are then categorized into three phases: a freely diffusive phase with a density ϕ_f (number per unit area), a bound phase to the ligands on the substrate with a density of ϕ_b, and a vacancy phase of density ϕ_v. The conservation of the total integrins in a cell holds in the static state, which is: $\int_\Omega(\phi_b + \phi_f)\mathrm{d}\Omega = \phi_0\Omega$ with ϕ_0 being a constant for a cell that covers an area of Ω. The three phases occupy all the sites on the cell membrane, satisfying the local conservation: $\phi_f + \phi_b + \phi_v = 1$. The mixture of the three phases brings an ideal entropy of mixing on the cell membrane, while the mismatch between different phases lead to gradient energies to the total chemical energy. In each focal adhesion point, the receptor-ligand pair is modeled as a linear spring with a spring constant k, the conjugate stretching force in the pair $\mathbf{F} = k\Delta\mathbf{u}$, and the stretching energy $\frac{1}{2}k(\Delta\mathbf{u})^2$. By forming each ligand-receptor pair, a certain amount of energy $\gamma = \mathbf{F} \cdot \Delta\mathbf{u}$ is released from the cell to stabilize the adhesion, which is an analogy to the pressure-volume term in the thermodynamics of gases. Amongst the three phases, only the bound phase ϕ_b is able to generate and transmit forces between the cell and

the substrate, therefore the traction force generated by the receptor-ligand pair and transmitted to the substrate is $\mathbf{T} = n_l\phi_b\mathbf{F}$, where n_l is the lattice site per unit area on the cell membrane. With the assumptions made above, the free energy of the cell membrane is written as:

$$\begin{aligned} W(\phi_f;\phi_b;\phi_v;\mathbf{u};\widehat{\mathbf{u}}) = &\int_\Omega n_l(\mu_f^0\phi_f + \mu_b^0\phi_b + \mu_v^0\phi_v)\mathrm{d}\Omega \\ &+ \int_\Omega n_l[\phi_b\ln\phi_b + \phi_f\ln\phi_f + \phi_v\ln\phi_v]\mathrm{d}\Omega \\ &+ \frac{1}{2}\int_\Omega[\beta_b(\nabla\phi_b)^2 + \beta_f(\nabla\phi_f)^2 + \beta_v(\nabla\phi_v)^2]\mathrm{d}\Omega' \\ &+ \frac{1}{2}\int_\Omega n_l\phi_b k|\Delta\mathbf{u}|^2\mathrm{d}\Omega - \int_\Omega n_l\phi_b\gamma\mathrm{d}\Omega \end{aligned} \tag{2-1}$$

where μ_f^0, μ_b^0, and μ_v^0 are the reference chemical potentials of the unbound and bound receptors, and vacuums, respectively; β_b, β_f and β_v are the gradient energy coefficients with respect to the three phases. The free energy consists of five parts: the chemical energy in the reference configuration, the entropic energy of three-phase-mixture, the gradient energies, the stretch energy stored in receptor-ligand bonds, and the energy released from the formation of receptor-ligand bond. All terms are in the unit of k_BT. By using the local conservation of the three phases, the gradient term in Eq. (1) can be rewritten as $\frac{1}{2}[(\beta_b+\beta_v)(\nabla\phi_b)^2 + (\beta_f+\beta_v)(\nabla\phi_f)^2 + 2\beta_v(\nabla\phi_b)(\nabla\phi_f)]$. For simplicity, we assume the isotropy of the gradient energy coefficient, leaving $\beta_b = \beta_f \equiv \beta n_l$ and $\beta_v = 0$. The total Gibbs free energy is then given as:

$$\Pi\big(\phi_b;\phi_f;\phi_v;\mathbf{u};\widehat{\mathbf{u}}\big) = W\big(\phi_f;\phi_b;\phi_v;\Delta\mathbf{u}\big) + \frac{h}{2}\int_\Omega \boldsymbol{\sigma}_{el}\colon\varepsilon_{el}\,\mathrm{d}\,\Omega + \int_{\partial\Omega}\Gamma\mathrm{d}\ell + \frac{1}{2}\int_V \widehat{\boldsymbol{\sigma}}_{el}\colon\hat{\boldsymbol{\varepsilon}}_{el}\mathrm{d}V, \tag{2-2}$$

where the first term is described by Equation (2-1). The second term is the elastic strain energy of the two-dimensional isotropic, elastic cell sheet with a thickness h, Young's modulus E and Poisson's ratio ν. We model the intracellular contraction by an active stress σ_A within the sheet, resembling the thermal cooling force and leading to the contractile thermal strain $-(1-\nu)\sigma_A/E$ in plane stress condition. Therefore, the elastic strain $\boldsymbol{\varepsilon}_{el}$ equals to $[\nabla\mathbf{u} + (\nabla\mathbf{u})^T]/2 + [(1-$

$\nu)\sigma_A/E]\mathbf{I}$, where $\mathbf{I}$ is the identity tensor. By applying the Hooke's Law of plane stress, the elastic stress in the cell is then written as:

$$\sigma_{ij}^{el} = \frac{E}{1-\nu^2}[\nu\,\delta_{ij}u_{k,k} + \frac{1-\nu}{2}(u_{i,j} + u_{j,i})] + \sigma_A\delta_{ij}, \tag{2-3}$$

The third term in Equation (2-2) is the line energy on the boundary of the cell sheet, where Γ is the line tension. The last term is the strain energy stored in the substrate. Now recall the constraint that the total number of integrins in the cell should be conserved, one then would write down the Lagrangian as:

$$L(\phi_b;\phi_f;\phi_v;\mathbf{u};\hat{\mathbf{u}};\lambda) = \Pi(\phi_b;\phi_f;\phi_v;\mathbf{u};\hat{\mathbf{u}}) + \lambda[\int_\Omega(\phi_b+\phi_f)\mathrm{d}\Omega - \phi_0\Omega], \tag{2-4}$$

where λ is the Lagrangian multiplier and is a constant. By noticing $\phi_f + \phi_b + \phi_v = 1$, we minimize the free energy functional (2-4) with respect to its independent variables ϕ_f and ϕ_b. It yields the partition of the receptors in the cell:

$$-\beta\,\nabla^2\phi_f + \ln[\phi_f/(1-\phi_f-\phi_b)] + \mu_f^0 - \mu_v^0 + \lambda = 0, \tag{2-5.1}$$

$$-\beta\,\nabla^2\phi_b + \ln[\phi_b/(1-\phi_f-\phi_b)] + \mu_b^0 - \mu_v^0 + \frac{1}{2}k(\Delta\mathbf{u})^2 - \gamma + \lambda = 0, \tag{2-5.2}$$

The boundary conditions are assumed for simplicity:

$$\nabla\phi_f\cdot\mathbf{n} = 0, \tag{2-6.1}$$

$$\nabla\phi_b\cdot\mathbf{n} = 0, \tag{2-6.2}$$

where $\mathbf{n}$ is the outer unit normal of the cell boundary. We further let $\Delta\mu^0 = \mu_b^0 - \mu_f^0$, and $\lambda' = \mu_f^0 - \mu_v^0 + \lambda$. One shall notice that $\gamma = k(\Delta\mathbf{u})^2$, therefore the above two equations can be simplified as:

$$-\beta\,\nabla^2\phi_f + \ln\left[\phi_f/\left(1-\phi_f-\phi_b\right)\right] + \lambda' = 0, \tag{2-7.1}$$

$$-\beta\,\nabla^2\phi_b + \ln\left[\phi_b/\left(1-\phi_f-\phi_b\right)\right] + \Delta\mu^0 - \frac{1}{2}\gamma + \lambda' = 0. \tag{2-7.2}$$

Using Equation (2-7.2) to subtract Equation (2-7.1), we can get the partition of the receptors in the cell:

$$\ln\left(\phi_b/\phi_f\right) - \beta\,\nabla^2\left(\phi_b-\phi_f\right) = \gamma/2 + \Delta\mu^0. \tag{2-8}$$

Equation (2-8) tells that once the system reaches its equilibrium, the chemical potential of ϕ_f and ϕ_b should be equal. Moreover, ϕ_b increases with $\gamma = \mathbf{F}\cdot\Delta\mathbf{u}$, indicating that the formation of focal adhesion actively responds to the mechanical force and traction forces promote the focal adhesion formation.

Minimizing the free energy functional with respect to the cell displacement field $\mathbf{u}$ gives rise to the mechanical equilibrium in the cell sheet.

$$\nabla\cdot\boldsymbol{\sigma}_{el} + Y\Delta\mathbf{u}/h = 0 \ \text{ in } \Omega, \tag{2-9}$$

where $Y = n_l k\phi_b$ is the effective focal adhesion strength, characterizing the coupling between the cell and the substrate. The traction force sustained in the focal adhesion points and transmitted to both the monolayer and the substrate is denoted by the term $Y\Delta\mathbf{u}$, which is averaged along the cell thickness and treated as a body force due to the two-dimensional landscape of the cell sheet. The cell is subjected to the traction boundary condition at its boundary:

$$\boldsymbol{\sigma}_{el}\cdot\mathbf{n} = -\frac{\Gamma\kappa}{h}\mathbf{n}, \tag{2-10}$$

where κ is the curvature of the cell boundary. Similarly, the substrate satisfies the mechanical equilibrium ($\nabla\cdot\hat{\sigma}_{el} = 0$) and surface traction boundary condition ($\mathbf{T} = Y\Delta\mathbf{u}$), and is modeled as elastic half space with a Young's modulus $\hat{E}$and Poisson's ratio $\hat{\upsilon}$. The solution to the mechanical equilibrium in the substrate can be solved from the Cerruti problem:

$$\hat{\mathbf{u}} = \int_{\Omega} \frac{1+\hat{\nu}}{\pi \hat{E} r^3} \begin{bmatrix} (1-\hat{\nu})r^2 + \hat{\nu} r_x^2 & \hat{\nu} r_x r_y \\ \hat{\nu} r_x r_y & (1-\hat{\nu})r^2 + \hat{\nu} r_y^2 \end{bmatrix} \begin{bmatrix} -Y\Delta \mathbf{u}_x \\ -Y\Delta \mathbf{u}_y \end{bmatrix} \mathrm{d}\Omega, \tag{2-11}$$

where $r_x = x - x'$, $r_y = y - y'$, $r = \sqrt{r_x^2 + r_y^2}$. By substituting Equation (2-8) into (2-10), one can get the displacement in the substrate expressed by the displacement in the cell:

$$\hat{\mathbf{u}} = \int_{\Omega} \frac{1+\hat{\nu}}{\pi \hat{E} r^3} \begin{bmatrix} (1-\hat{\nu})r^2 + \hat{\nu} r_x^2 & \hat{\nu} r_x r_y \\ \hat{\nu} r_x r_y & (1-\hat{\nu})r^2 + \hat{\nu} r_y^2 \end{bmatrix} \begin{bmatrix} h(\sigma_{el})_{xx,x} + h(\sigma_{el})_{xy,y} \\ h(\sigma_{el})_{xy,x} + h(\sigma_{el})_{yy,y} \end{bmatrix} \mathrm{d}\Omega. \tag{2-12}$$

Equations (2-5) to (2-12) manifest highly nonlinear coupling between the cell and the substrate, for which analytical solution is not available. We implement the model into the finite element method, which simultaneously yields the focal adhesion distribution, the traction force landscape, and the cell body stress profile.

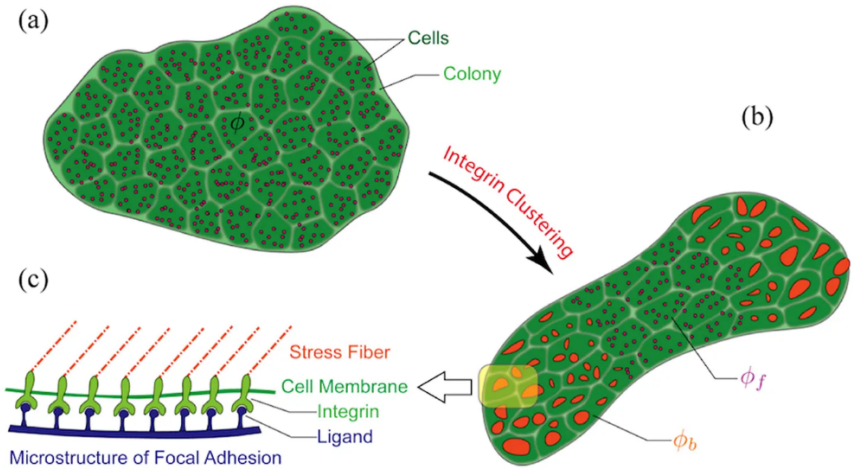

Fig. 2.2. Schematics of force generation mediated by focal adhesion formation through integrin clustering in a multicellular monolayer. (a) Randomly distributed, freely diffusive integrins (red dots) on cell membrane. (b) Focal adhesion formation through integrin clustering upon cell-substrate interactions. (c) Molecular structure of the focal adhesions.

The model can be extended to HCT-8 epithelial cell colonies (a colony consists of hundreds of cells packed together through cell-cell adhesion.), as an example of cohesive multicellular monolayers. They are seeded onto polyacrylamide (PAA) gels in vitro. They proliferate and aggregate to form cohesive multicellular monolayers of different sizes and morphologies (Fig. 2.2). Once they sense mechanical cues from substrate through integrin receptors, the myosin motors are activated, and the cellular contractility will increase, and in-turn facilitates the integrin clustering to promote focal adhesion formation and cytoskeletal assembly. The contractility will then help generate the traction force and intercellular tension. Same with the single cell case, the integrin receptors on the cell colony membrane are categorized into three distinct phases: a freely diffusive phase with a density of $\phi_{i,f}$, a bound phase to the ligands on the substrate with a density of $\phi_{i,b}$, and a vacancy phase with density $\phi_{i,v}$ for the *i*-th cell in the colony. Conservation of the total number of the receptors on the membrane with respect to the *i*-th cell leads to the equation: $\int_{\Omega_i}(\phi_{i,b}+\phi_{i,f})\mathrm{d}\Omega_i = \phi_{\mathrm{i},0}\Omega_i$, with $\phi_{\mathrm{i},0}$ being a constant for the *i*-th cell that covers an area of Ω_i. The summation of the three phases conserves point-wisely on the cell membrane: $\phi_{i,f}+\phi_{i,b}+\phi_{i,v}=1$.The energy associated with receptors is rewritten with respect to the *i*-th cell:

$$\begin{aligned}\widehat{W}_i(\phi_{i,f};\phi_{i,b};\phi_{i,v};\mathbf{u};\widehat{\mathbf{u}}) = &\int_{\Omega_i} n_l(\mu_{i,f}^0\phi_{i,f}+\mu_{i,b}^0\phi_{i,b}+\mu_{i,v}^0\phi_{i,v})\mathrm{d}\Omega_i\\ &+\int_{\Omega_i} n_l[\phi_{i,b}\ln\phi_{i,b}+\phi_{i,f}\ln\phi_{i,f}+\phi_{i,v}\ln\phi_{i,v}]\mathrm{d}\Omega_i\\ &+\tfrac{1}{2}\int_{\Omega_i}[\beta_{i,b}(\nabla\phi_{i,b})^2+\beta_{i,f}(\nabla\phi_{i,f})^2+\beta_{i,v}(\nabla\phi_{i,v})^2]\mathrm{d}\Omega_i\\ &+\tfrac{1}{2}\int_{\Omega_i} n_l\phi_{i,b}k|\Delta\mathbf{u}|^2\mathrm{d}\Omega_i-\int_{\Omega_i} n_l\phi_{i,b}\gamma\mathrm{d}\Omega_i\end{aligned}. \quad (2\text{-}13)$$

The free energy functional of the cohesive monolayer takes the following form:

$$\Pi(\phi_b;\mathbf{u};\widehat{\mathbf{u}}) = \sum_i^N \widehat{W}_i\left(\phi_{i,f};\phi_{i,b};\phi_{i,v};\Delta\mathbf{u}\right)+\tfrac{h}{2}\int_\Omega \sigma_{el}:\boldsymbol{\varepsilon}_{el}\,\mathrm{d}\,\Omega+\int_{\partial\Omega}\Gamma\mathrm{d}\ell+\tfrac{1}{2}\int_V\widehat{\boldsymbol{\sigma}}_{el}:\hat{\boldsymbol{\varepsilon}}_{el}\mathrm{d}V, \quad (2\text{-}14)$$

where the first term is the summation of the free energies associated with the receptors of all the constituent cells, and the next three terms are constructed on the continuum level without

differentiating individual cells. The constitutive law for cells and substrate takes the same form with the single cell case. Now recall the constraint that the total number of integrins in each cell should be conserved, one then would write down the Lagrangian as:

$$L(\phi_b; \mathbf{u}; \hat{\mathbf{u}}; \lambda) = \Pi(\phi_b; \mathbf{u}; \hat{\mathbf{u}}) + \sum_i^N \lambda_i [\int_{\Omega_i} (\phi_{i,b} + \phi_{i,f}) \mathrm{d}\Omega_i - \phi_{i,0}\Omega_i], \quad (2\text{-}15)$$

where $\lambda = \lambda_i$ is the Lagrangian multiplier for the *i*-th cell. Minimizing the free energy functional with respect to its independent variables yields the partition of the receptors in each cell:

$$-\beta\, \nabla^2 \phi_{i,f} + \ln[\phi_{i,f}/(1 - \phi_{i,f} - \phi_{i,b})] + \lambda_i{}' = 0 \text{ in the } i\text{-th cell}, \quad (2\text{-}16.1)$$

$$-\beta\, \nabla^2 \phi_{i,b} + \ln[\phi_{i,b}/(1 - \phi_{i,f} - \phi_{i,b})] + \Delta\mu^0 - \frac{1}{2}\gamma + \lambda_i{}' = 0 \text{ in the } i\text{-th cell}, \quad (2\text{-}16.2)$$

where $\Delta\mu^0 = \mu_{i,b}^0 - \mu_{i,f}^0$, $\lambda_i{}' = \mu_{i,f}^0 - \mu_{i,v}^0 + \lambda_i$,and $\gamma = k(\Delta\mathbf{u})^2$. The boundary conditions are assumed for simplicity:

$$\nabla\phi_{i,f} \cdot \mathbf{n}_i = 0 \text{ on the boundary of the } i\text{-th cell}, \quad (2\text{-}17.1)$$

$$\nabla\phi_{i,b} \cdot \mathbf{n}_i = 0 \text{ on the boundary of the } i\text{-th cell}, \quad (2\text{-}17.2)$$

where $\mathbf{n}_i$ is the outer unit normal of the boundary of the *i*-th cell. We note that the expression of the stress equilibrium and the corresponding boundary condition of the cohesive monolayer remain unchanged, so do the stress equilibrium and the surface boundary condition of the substrate.

2.3. Numerical implementation

Apply weak form in COMSOL

Due to the nonlinearity of the system and the irregular geometry of the cells, we apply finite elements method to solve the equations. Firstly, we write Equation (2-5~7) and Equation (2-9~10) into the weak form:

$$\int_\Omega \beta(\nabla\phi_f)\cdot(\nabla\tilde{\phi}_f)+\{\ln[\phi_f/(1-\phi_f-\phi_b)]+\lambda'\}\tilde{\phi}_f \mathrm{d}\Omega-\int_{\partial\Omega}\tilde{\phi}_f\nabla\phi_f\cdot\mathbf{n}\mathrm{d}l=0, \quad (2\text{-}20.1)$$

$$\int_\Omega \beta(\nabla\phi_b)\cdot(\nabla\tilde{\phi}_b)+\{\ln[\phi_b/(1-\phi_f-\phi_b)]+\Delta\mu^0-\frac{1}{2}\gamma+\lambda'\}\tilde{\phi}_b \mathrm{d}\Omega-\int_{\partial\Omega}\tilde{\phi}_b\nabla\phi_b\cdot\mathbf{n}\mathrm{d}l=0, \quad (2\text{-}20.2)$$

$$\int_\Omega[\boldsymbol{\sigma}_{el}\cdot(\nabla\tilde{\mathbf{u}})_{sym}-Y\Delta\mathbf{u}\cdot\tilde{\mathbf{u}}/h]\mathrm{d}\Omega-\int_{\partial\Omega}(-\Gamma\kappa/h\tilde{\mathbf{u}}\cdot\mathbf{n})\mathrm{d}\ell=0, \quad (2\text{-}20.3)$$

where "~" means the test functions, and λ' is obtained by solving $\int_\Omega(\phi_b+\phi_f)\mathrm{d}\Omega=\phi_0\Omega$. We implement Equation (2.3) and (2-12) ~ (2-13) into the commercial package COMSOL. For cell colonies, Equation (2-20.1) and (2-20.2) should be applied for each cell inside the colonies. A ten-node cubic triangle element is used to generate the mesh. For single cells, the mesh size is $1\sim2\mu m$. The number of elements is in the order of 10^3; the total number of the degree of the freedom is in the order of 10^4. For cell colonies, the mesh size is around $2.5\sim10\mu m$, as the radius of the colony increases from $50\mu m$ to $200\mu m$. The number of elements is still in the order of 10^3; the total number of the degree of the freedom is in the order of 10^4. We use default settings in the solver to solve the equations along with boundary conditions in a fully coupled manner. Parallel computing is used for 20 CPUs. The total solution time takes about 3~4 hours.

.

Parameter settings and validations

In this section, we will discuss how we choose parameters which make sense in physics for our model. Firstly, we assume that the parameters in our model are mainly cell-type dependent, meaning the same kind of cell or cell colonies shares roughly the same parameters. Next, since some of the parameters are difficult to measure by experiment, we will firstly give the order of the magnitude of the parameter. The exact values of the parameters are then determined by matching our prediction on the traction force landscape with the experiment results of real cells. The parameters used for the single cells and cohesive colonies in Chapter 3 are listed in Appendix A.

Firstly, we determine the material parameters and the geometry parameters for the cells. For Young's modulus and Poisson's ratios of cells, previous studies show that they are usually in the range of $10^3 \sim 10^4$Pa and $0.4 \sim 0.5$, respectively [18-20, 40]. Therefore, we set the Young's modulus for NIH 3T3 cells and SaOS-2 cells to be about 5kPa. While for HCT-8 colonies, the Young's modulus is around 10kPa. The thicknesses of the cell sheet and the HCT-8 are directly measured from the experiment. For NIH 3T3 cells and SaOS-2 cells, it is about $3 \sim 4\mu$m, while for HCT-8 colony, the average thickness is about 12.5μm.

Next, we determine the parameters associated with the receptors. The cell membrane is mainly made by lipids, where the integrin receptors only take a small portion of it. The portion of the freely diffusive integrins and bound ones should not exceed 10^{-1}, therefore we have $\phi_0 \leq 0.1$. As a result of it, the portion of the vacancy is about 10^1 times of the integrins. And in the reference configuration where there is zero displacement, the partition of different phases

follows $\frac{\phi_b}{\phi_f} \sim e^{-\Delta\mu^0/k_BT}$. By noticing that $\frac{\phi_b}{\phi_f} \sim 10^{-2}$ in the reference configuration, the values of $\Delta\mu^0$ should be about a few k_BTs [23]. We then notice that the stretch $|\Delta\mathbf{u}|$ in the ligand-receptor bond for small deformation model is about a few microns and the stretching energy in it is around $10^0 \sim 10^1 k_BT$ [41]. Therefore, the spring constant k can be roughly determined. The lattice number n_l is around $10^5 \sim 10^6 \mu\text{m}^{-2}$ so that the effective coupling strength Y is in the order of magnitude of 10^9N/m^3. The coefficient of the gradient energy β is determined to make the interfaces of different phases to be diffusive. The line tensions for single cells are determined by matching the predicted traction force with the experimental results with respect to cells in different morphologies, and we note that based on previous studies, the line tensions for single cells should be in the order of $10^{-9} \sim 10^{-8} \text{J/m}$ [42]. The line tension for HCT-8 colonies are determined by matching the predicted traction force with the experimental results with respect to patterned circular colonies of different sizes based on previous work.

All the above-mentioned parameters that cannot be measured directly from experiments or be found from previous studies are validated by matching the predictions with the experiments for cells and colonies as many as possible. For patterned NIH 3T3 cells, we simulated around 15 cells in total; for irregular-shaped SaOS-2 cells, we simulated around 10 cells in total; for patterned and non-patterned HCT-8 colonies, we simulated around 50 in total. Part of the simulation results will be presented in the next chapter. We address here: due to the limit in the number of the experimental samples, this is the best we can do to validate the correctness of our parameters currently. In the future work, we will apply this model to predict the traction forces for about 10^2 cells and colonies. These results will be the samples of the new machine learning

approach to predict traction forces of cells and cell colonies. The validation of the current parameter settings also will be fully conducted.

2.4. Conclusion and summary

A thermodynamic model considering both the force equilibrium in cells and substrate and the chemical equilibrium in integrin partition has been developed in this chapter. The free energy functional is formulated with respect to the displacement in the cell and the substrate, and the density of free and bound integrins. By applying the variational theorem, we obtain the governing equations and boundary conditions. To solve the boundary value problem, we rewrite the governing equations and boundary conditions in the weak form and implement them in COMSOL. The parameters should be calibrated by matching the predicted results with experiment measurements.

Chapter 3

Applications of the thermodynamic model to single cells and cohesive monolayers

3.1. Introduction

In this chapter, we apply our model developed in Chapter 2 to predict the force generation and transmission, and the focal adhesion formation for single cells and cohesive colonies. We first present the substrate stiffness dependent active contractility for NIH 3T3 cells and HCT-8 colonies. We then examine the geometry regulated traction force landscape and the focal adhesion profile for single SaOS-2 cells, and the geometry regulated cellular stress landscape for cells patterned on glass. Next, we predict the reciprocal cell-matrix coupling, the colony size and gel stiffness dependent traction force maps in HCT-8 colonies. At last, the traction force mediated metastatic-like dispersion are presented to show the wide application of our model.

3.2. Intracellular contractility depends on substrate stiffness

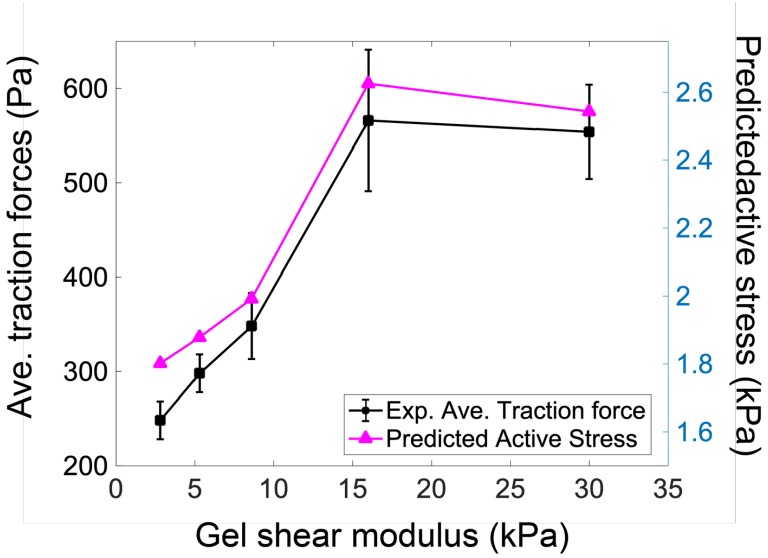

Fig. 3.1. Average substrate traction stress, as measured experimentally (black squares) and predicted active stress by data matching (magenta triangles), versus substrate shear elastic modulus. Error bars represent standard error of the mean. Experimental data are from [21]. The model parameters are listed in Table. A.1 in Appendix A.

A contractile cell can sense the substrate stiffness and respond by modulating its contractility and cytoskeletal remodeling [43]. Here, a substrate-stiffness-dependent parameter, called the active stress σ_A, is adopted to measure the cellular contractility. To determine how the value of active stress varies with respect to the substrate stiffness, we apply our model to simulate the traction force landscapes of the patterned circular NIH 3T3 cells from previous studies [21]. The model parameters for NIH 3T3 cells can be found in Table A.1 in Appendix A. By matching the simulated average traction forces with the experiment measurements, we can determine the active stress σ_A corresponding to the hydrogel stiffness. Our data matching shows that the active stress firstly increases with the hydrogel shear elastic modulus from 2.8kPa to 8.6kPa, manifesting a positive feedback in mechanical sensing and force generation in contractile cells. The active stress then

saturates when the hydrogel shear elastic modulus reaches 16kPa. After the saturation point, the active stress slightly drops for cells on gels with the 30kPa shear modulus. This drop suggests that once the substrate stiffness reaches a threshold, the active stress should also saturate around the maximum value.

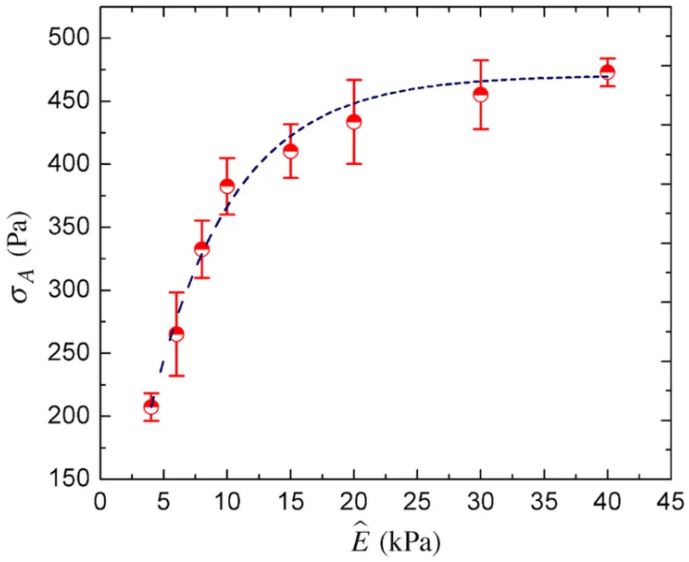

Fig. 3.2. Substrate stiffness mediates cell contractility. Active stress versus Young's modulus of substrate $\hat{E}$ obtained by experimental-numerical matching of the traction forces. The model parameters are listed in Table. A.2 in Appendix A.

The substrate-stiffness-dependent contractility also holds for cohesive monolayers. The HCT-8 monolayers of roughly the same radius R ~150μm are studied on hydrogels with different stiffness. The maps of traction force of the colonies are firstly measured by TFM, then the average traction force within a 50μm boundary layer is recorded. We also predict the traction force profile by the thermodynamic model with assumed active stress and calculate the average traction force within the same boundary layer. The model parameters for HCT-8 colonies can be found in Table A.2 in

Appendix A. The active stress for different gel stiffness is then determined by matching the numerical results with the experimental measurements. The matching results show that the active stress monotonically increases with the gel stiffness and nearly stops increasing when the substrate Young's modulus reaches 30kPa [44, 45]. The saturation in the active stress manifests the limit of cell internal machinery in driving crosslinking actomyosin motors.

3.3. Geometry regulated traction force landscape and focal adhesion distribution for single cells

In this section, we simulate the traction force landscape of the SaOS-2 cells with different morphologies seeded on hydrogels. The model parameters for SaOS-2 cells can be found in Table. A.1 in Appendix A. Figure 3.3 shows the predicted extracellular tractions for cells with different geometries, which are in good comparison with the experimental data. By looking carefully into Figure 3.3, one can see that the boundary curvature totally governs the traction force distribution for arbitrary shaped cell. At the convex boundaries with positive curvatures, the line tension generates an effective inward pressure on the cell, which needs extra traction forces to counter-balance. Therefore, traction forces concentrate at convex boundaries. While at the concave boundaries with negative curvatures, the line tension generates an effective outward pulling force on the cell, which negates the cellular contractility. Therefore, traction forces vanish at concave boundaries.

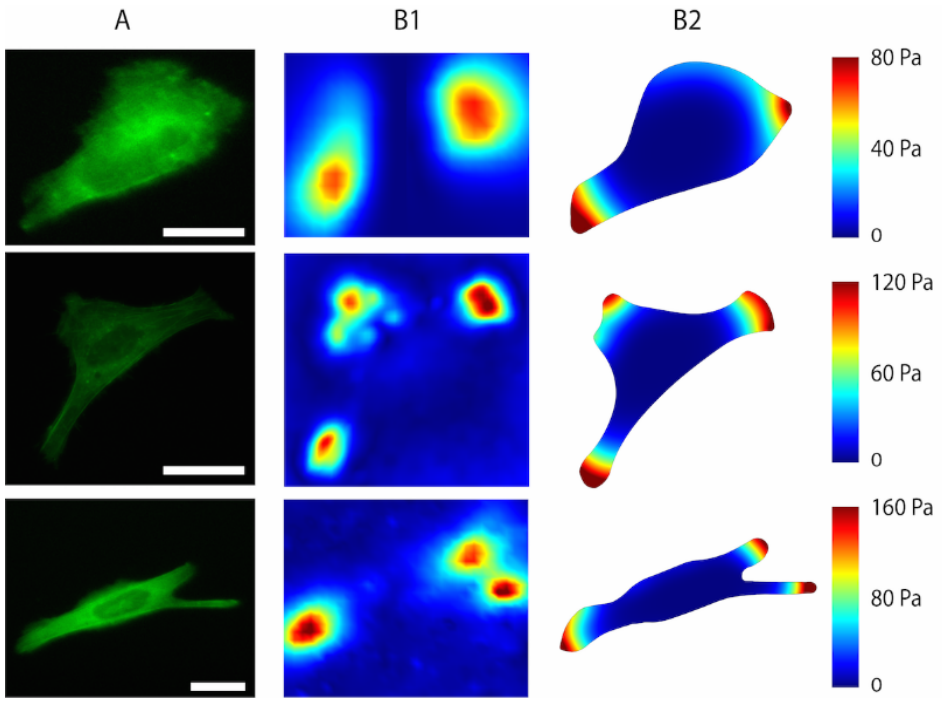

Fig. 3.3. Traction force is regulated by the cellular geometry. Column A: Phase contrast images of SaOS-2 cells on different gel Young's modulus (from top to bottom: 4kPa, 10kPa and 20kPa, respectively; scale bar: 30μm). Column B1~B2: The traction force profiles of the cells obtained from experiments and modeling, respectively. The model parameters are listed in Table. A.1 in Appendix A.

We next stain the actin filaments and focal adhesion kinase (FAK) for a single SaOS-2 cell, shown in Figure 3.4. One can see that the stress fibers (Fig.3.4 (a)) connect the focal adhesion points in Fig. 3.4 (b). In Fig. 3.4 (c), we plot the predicted first principal stress by color contour and its directions by arrows. The directions of the first principal stress highly align with the stress fibers. In Fig. 3.4. (b), same as traction forces, the focal adhesions concentrate at the convex boundaries and vanish at the concave boundaries, which is also predicted by our simulation in Fig. 3.4 (d).

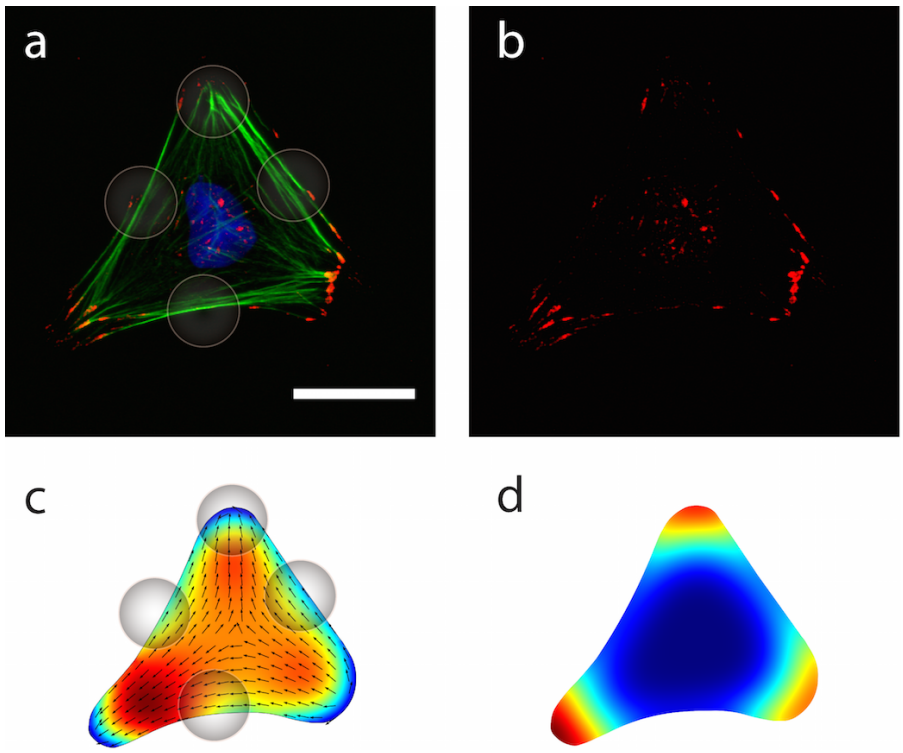

Fig. 3.4. Focal adhesion (represented as the stained FAK) and stress fiber distribution. (a) Stained stress fiber and FAK. (b) Stained FAK. (c) Predicted first principal stress by color contour and its direction by arrow. Red means large and blue means small. Stress fiber directions align with the maximum principle stress, marked by the semi-transparent circles. (d) Predicted focal adhesion distribution. Red means the higher density and blue means lower density.

3.4. Geometry regulated nanoparticle uptake of patterned cells on glass

Cellular uptake of nanoparticles (NPs) has been an extensively studied topic over the last several decades because of its application in developing the next-generation medicine that allows early-stage cancer detection, and simultaneous diagnosis and treatment of pathological conditions [46, 47]. Enormous efforts have been devoted into this area to improve the targeting efficiency and to minimize the toxicity, yet it still remains an imperative challenge to develop NP-uptake

technology with such requirements .It is shown recently that the effect of the surface mechanics of cells, such as membrane tensions, should not be neglected in cellular uptake of NPs [48-51]. Recently, our group calculate the tensions inside the cohesive monolayers on deformable gels with different stiffness by the Monolayer Stress Microscopy (MSM) and then correlate the cellular tensions with the number of NP-uptake per unit area [52]. It shows that the uptake of NPs decreases as the cellular tension increases. For cells adhering on rigid substrate, such as glass and bones, the Traction Force Microscopy (TFM) becomes useless. Our model then becomes the ideal tool to predict the intracellular tension and build a correlation between the cellular tension and the NP-uptake.

In this section, NIH 3T3 cells are patterned with the same area ($\sim 2500\ \mu m^2$) but with different aspect ratios on glass. NPs are delivered into the cells and the numbers are calculated with respect to each cell. As shown in Figure 3.5, both the experiment and simulation show that the focal adhesions aggregate at the corners of the cells. We also get the cellular stress and traction force profile, presented in Figure 3.6. From the simulation, one can see that the magnitude of the traction forces remains almost unchanged while the aspect ratio is changing. However, despite the unchanged traction forces, the internal stress of the cells increases rapidly as the aspect ratio increases from 1.5 to 8. This is a good example that shows the influence of cellular geometry on cell internal stress. We then calculate the average internal stress for different aspect ratios and the results are listed in Table 2.1 and 2.2. We find that the average internal stress in the central region of the cells first decreases as the aspect ratio goes from 1 to 1.5, and then increases as the aspect ratio goes from 1.5 to 8. A strong correlation is then revealed between the internal stress and the NP-uptake number. As the stress first goes down, the NP-uptake number increases and

reaches the maximum when the aspect ratio equals to 1.5. Then the NP-uptake number decreases as the aspect ratio continues to increase. We note here, the cell contractility reaches its maximum on rigid substrate, therefore, the shape of the cell, instead of substrate stiffness, becomes the key factor that determine the value of cellular tension.

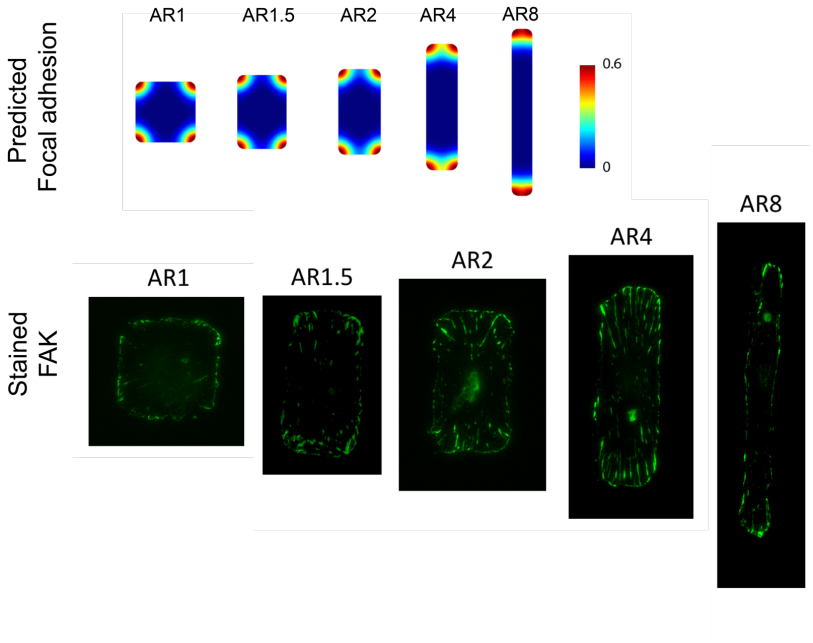

Fig. 3.5. Top row: focal adhesion distribution versus different aspect ratios predicted by our thermodynamic model; bottom row: focal adhesion distribution versus different aspect ratios by experiment. Model parameters are listed in Table. A.1 in Appendix A.

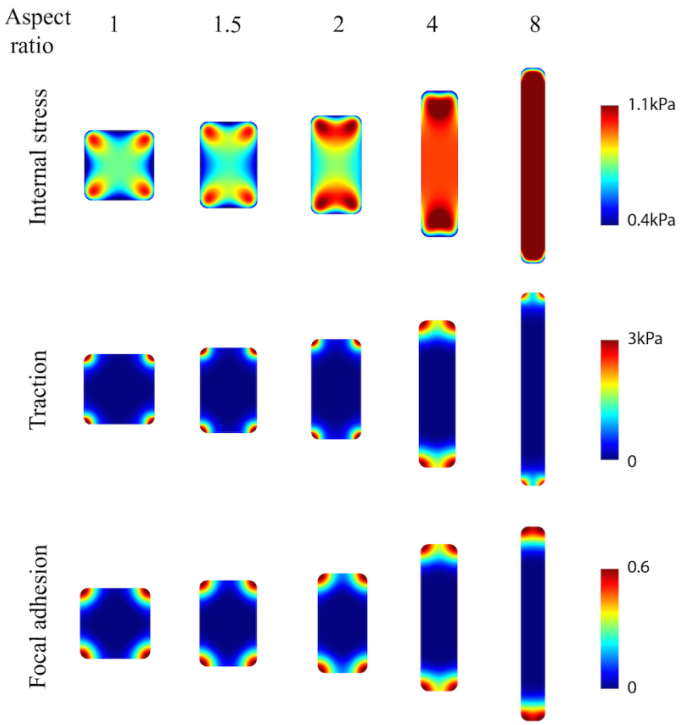

Fig. 3.6. Predictions made by the thermodynamic model. Top row: internal stress profile versus different aspect ratios; middle row: traction force landscape versus different aspect ratios; bottom row: focal adhesion distribution versus different aspect ratios.

Average stress (Pa)	Aspect Ratio
715.95	1
724.36	1.5
826.81	2
926.29	4
1462.9	8

Tab. 2.1. The average internal stress in the whole cell vs. aspect ratio.

Average stress (Pa)	Aspect Ratio
746.90	1
726.09	1.5
816.25	2
972.86	4
1533.9	8

Tab. 2.2. The average internal stress in the central region of the cell (occupies the 1/4 of the total area) vs. aspect ratio.

3.5. Active, nonlinear cell-matrix coupling of HCT-8 colonies

Like a thin film shrinking in-plane under thermal cooling, the displacement field led by the intracellular contractility in the HCT-8 cell monolayer monotonically decreases in magnitude from the periphery to the center, as shown in Figure 3.7. The intracellular contraction generates traction forces, which are transmitted onto the substrate by focal adhesions. Since the traction forces are

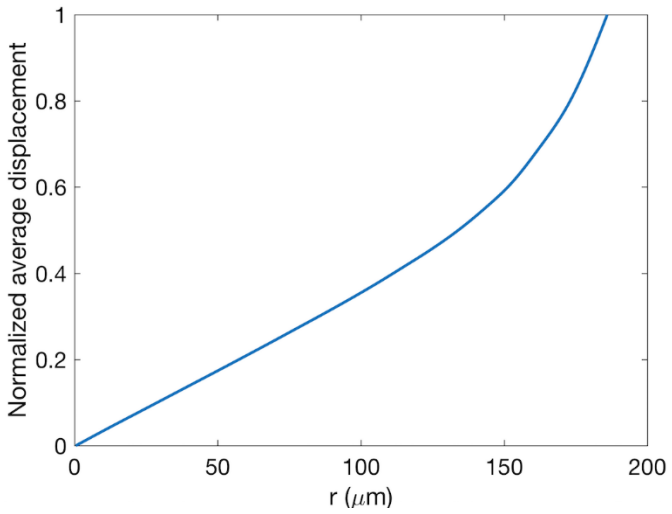

Fig. 3.7. The decay of the magnitude of displacement from the periphery to the centroid of HCT-8 colony of 186μm in radius, predicted by the models, normalized by the maximum value.

proportional to the displacement, they share the same spatial profile as the displacement field has ($|\mathbf{T}| \sim |\Delta\mathbf{u}|$): to be high at the periphery and low at the center of the monolayer. Since $|\mathbf{F}|$ is also proportional to $|\Delta\mathbf{u}|$, the tensions in the ligand-receptor pairs at the periphery of the monolayer are relatively higher than those in the centroid. Such high tensions promote integrin clustering (increasing ϕ_b) and stabilize focal adhesion points, as indicated by Equation (2-8). The large ϕ_b further leads to the large traction forces at the periphery as the traction forces are proportional to ϕ_b. The traction forces are then transmitted back to the monolayer through the ligand-receptor pairs, establishing the cellular stress. As shown in Figure 3.8 (a) and (b), the focal adhesions and traction forces of the HCT-8 monolayers co-localize within the periphery whose width is about 50μm due to such interactive coupling. The results are obtained by both the immunofluorescence of the focal adhesion kinase (FAK) and traction force microscopy (TFM), respectively. The width that spans roughly 5 HCT-8 cells, which is called the boundary layer.

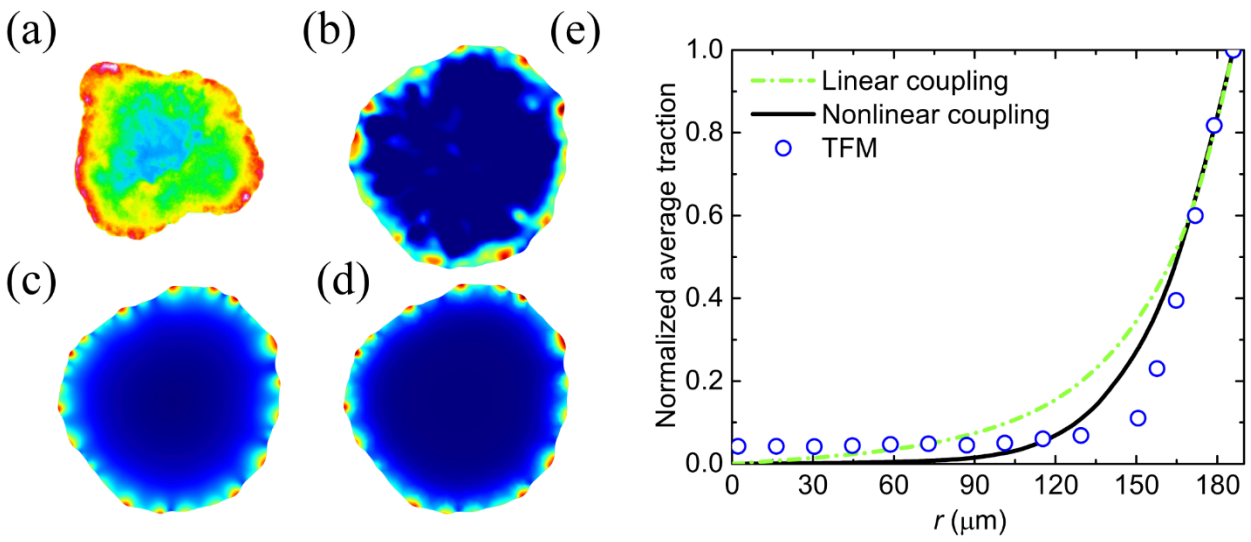

Fig. 3.8. Nonlinear reciprocal cell-matrix coupling. Left: (a) Immunofluorescence staining shows localization of focal adhesion kinase (FAK) at the boundary layer of a monolayer. (b) The traction force map measured by TFM. (c)-(d) The traction force maps predicted by the previous uniform coupling model (c, constant Y) and the current nonlinear coupling model (d, nonlinear Y) model, subtracted by the map from TFM in (b). The darker the pixel, the better the agreement of the traction force. (e) The decay of the radial component of traction force from the periphery to the centroid of HCT-8 colony of 186 μm in radius, shown in (b), predicted by the models and TFM. All the results are normalized by the maximum average radial traction forces.

The coupling strength between the monolayer and the substrate, characterized by Y, is also highly nonlinear (Figure 3.9), which arises from the nonlinear dependence of ϕ_b on the stretch $|\Delta\mathbf{u}|$. This conclusion contrasts with the assumption of uniform coupling (constant Y in space) in previous models [18-21]. Our theoretical study below on circular shaped monolayer with radius R shows that the traction force landscape is governed by the characteristics of monolayer-substrate coupling. For uniform coupling, the radial displacement of the circular monolayer decays with a modified Bessel function, $u_r \sim I_1(r/R)$, so does the traction force [18]. In contrast, for the nonlinear coupling derived here, the decay of the radial displacement can be approximated by the derivative of the

Airy function of the second kind, $u_r \sim (\frac{R}{r}) A_2'(r/R)$, and the traction force by $A_2'(r/R)$. This conclusion is derived by assuming focal adhesions are only formed within the boundary layer of a characteristic width Δ and the focal adhesion density in the boundary layer is linearly increasing in the radial direction. The mechanical equilibrium in the boundary layer therefore requires:

$$r^2 \frac{\partial^2 u_r}{\partial r^2} + r \frac{\partial u_r}{\partial r} - [1 + \frac{n_l k \phi_{i,0} r^3 (1-\upsilon^2)}{\Delta E h}] u_r = 0. \quad (3\text{-}14)$$

By solving the equilibrium equation, one finds that the displacement decays by the derivative of Airy function of the 2nd kind:

$$u^c \sim \frac{A_2'[(\frac{n_l k \phi_{i,0}}{E h \Delta})^{1/3} r]}{r}. \quad (3\text{-}15)$$

The traction force is then approximated as

$$T \sim \frac{n_l k \phi_{i,0}}{\Delta} A_2'[(\frac{n_l k \phi_{i,0}}{E h \Delta})^{1/3} r]. \quad (3\text{-}16)$$

This decay is faster than that under uniform coupling, because of the stronger localization of the traction forces and focal adhesions inside the boundary layer. The traction force maps of an irregularly shape monolayer, predicted by the uniform coupling model and the current nonlinear model are presented in Figure 3.8. The difference between the results predicted by the models is clearly seen in Figure 3.8 (e). All the data points are measures of the average over the small region $(r - \delta, r + \delta)$, where *r* is the radial distance from the current location to the colony centroid, and $\delta \ll R$. The current nonlinear model (solid black line) predicts a faster decay of the traction force from the periphery to the centroid of the monolayer than the uniform coupling model (dashed green line), which is consistent with the theoretical analysis and has a better agreement with the experimental results from TFM (open circles).

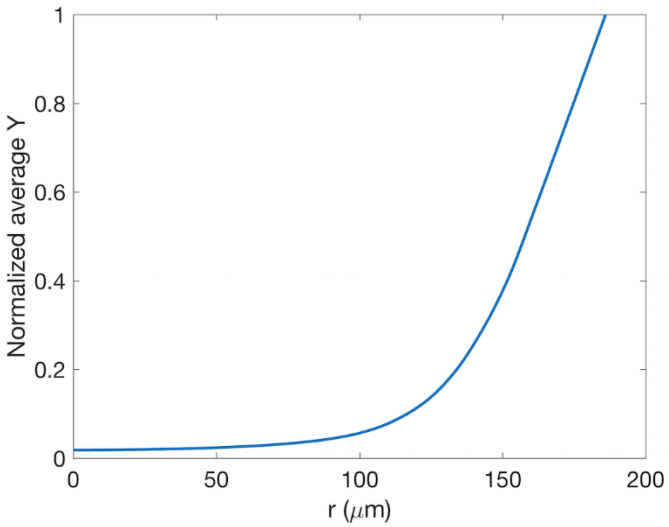

Fig. 3.9. The distribution of coupling strength from the periphery to the centroid of HCT-8 colony of 186μm in radius, predicted by the models, normalized by the maximum value.

3.6. Intracellular traction and intercellular tension are both gel stiffness and colony size dependent

In this section, we apply our model to simulate the traction force profiles of the monolayers with different sizes and on substrates of different stiffness, as shown in Figure. 3.10 (a1) and (a2) for the phase contrast images. The traction force map of the colonies is measured by TFM. The comparison between TFM and our simulations shows that our model captures the overall traction map remarkably well, as shown in Figure. 3.10, (c1) and (c2). Owing to the active cell-substrate coupling described above, traction forces are highly localized within the boundary layer, same as the localization of the focal adhesions. Arising from the stiffness-dependent cell contractility, the model predicts that the traction force is gel stiffness dependent (Figure 3.10, (c1)). The predicted average traction forces over the boundary layers of ~50 μm in width are 61.7Pa, 105.3Pa, and

138.6Pa for the colonies on 4.5kPa, 20.7kPa, and 47.1kPa gels, respectively. At the periphery of the colonies, the traction forces concentrate at the location with high curvature while vanish at the location where there is a negative curvature. This is because of the existence of the line tension acting on the boundaries of the colonies. Same as the role it plays for single cells, the line tension induces an effective inward pressure that requires more traction forces to counterbalance where the boundary is convex with positive curvatures. This leads to another conclusion that the traction force is also colony size dependent since colonies with different sizes have different overall curvatures. And indeed, the model predicts that the traction force is size dependent (Figure 3.10, (c2)). Specifically, the average traction forces within the 50μm thick boundary layer are 117.2Pa, 109.8Pa, and 105.3Pa for 54μm, 107μm 186μm colonies, respectively.

The cellular stress obtained from MSM and the simulation is plotted in Figure 3.10, (d1) and (d2). Opposite to the traction force profile, the cellular stress is minimal at the periphery of the cell sheet, ramps up over the boundary layer, and finally reaches a uniform tension. This opposite correlation arises from the way that how cellular stress is transmitted. At the boundary layer, the cell contraction is transmitted through the focal adhesions, where the cellular stress is mostly balanced with the traction forces. As the traction forces decay from its maximal to zero, the cellular tension increases from its minimal to its maximal. Hence at the interior of the cell sheet, there is no extracellular traction generated, cellular stress is mostly transmitted to the neighboring cells through cadherin-based cell-cell junctions. As a result of it, the stress/tension at the interior tends to be uniform. In conclusion, cellular stress scales with the gel stiffness (Figure 3.10, (d1) and (e1))

and the colony size (Figure. 3.10, (d2) and (e2)) in the similar way with the traction force at the boundary layer of the colonies, which is confirmed by both our simulation results and MSM results.

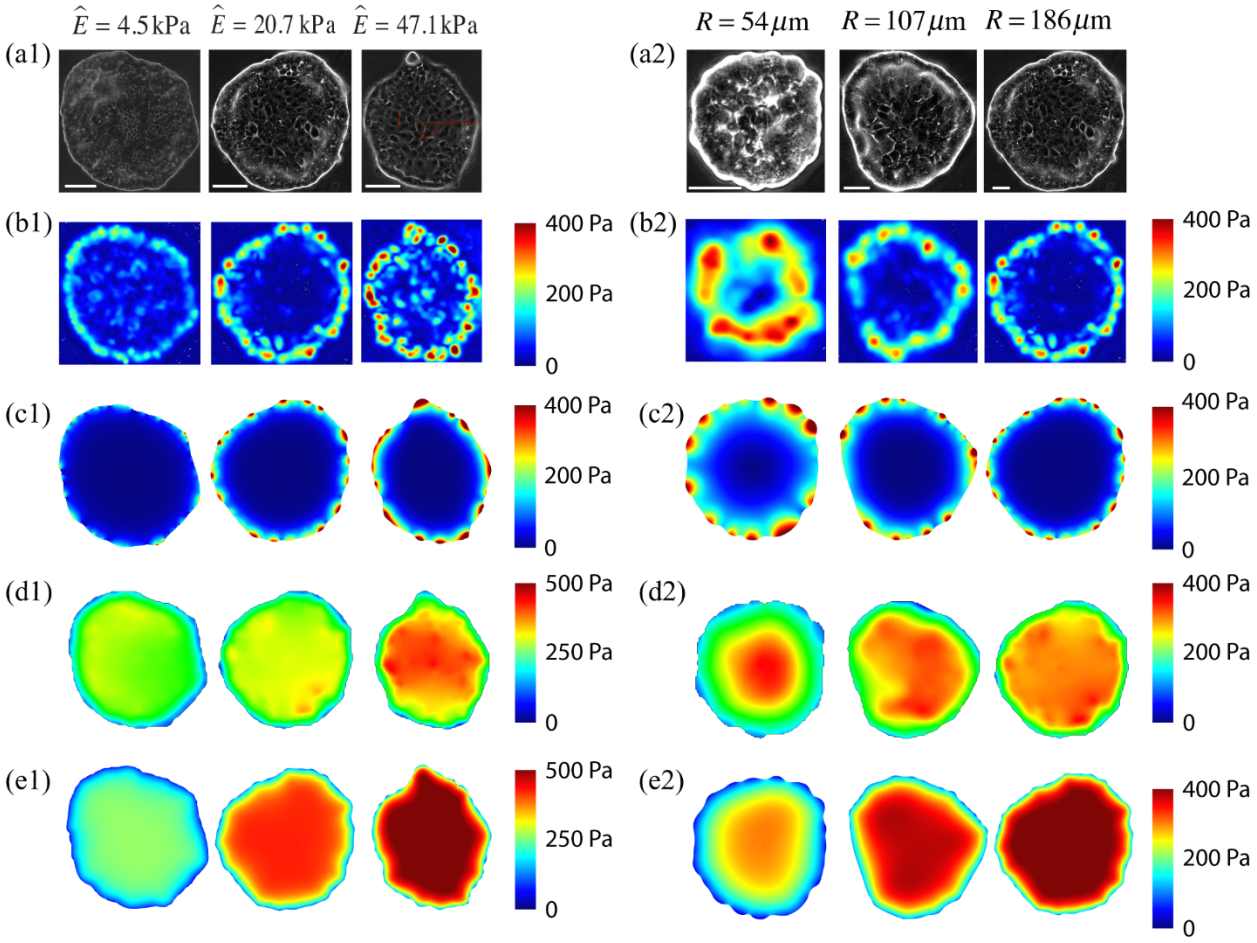

Fig. 3.10. Traction force is both substrate stiffness (Left panel) and colony size (Right panel) dependent. (a1-a2): Phase contrast images of HCT-8 cell colonies on different gel stiffness (a1,with gel stiffness of 4.5kPa, 20.7kPa and 47.1kPa, respectively; scale bar: 90μm) and with different monolayer sizes (a2, scale bar: 45μm) on 20.7kPa gels. (b-c) The traction force profiles of the cell colonies obtained by TFM (b1-b2) and modeling (c1-c2), respectively. (d-e) The intercellular tension maps of the cell colonies obtained by MSM (d1-d2) and modeling (e1-e2). The model parameters are listed in Table. A.2 in Appendix.

3.7. Cellular-force threshold exists at pre-dispersion stage for the dispersion behavior

Cancer metastasis is an enormously complicated process which is triggered by vascularization of a primary tumor. Cancer cells detach from the primary tumor and enter the blood vessels. They travel though blood vessels, extravasate from blood vessels at somewhere, and proliferate into a secondary tumor. Tremendous efforts have been carried out to identify possible biochemical markers for the onset of metastasis. Recent studies have shown accumulative evidence that the onset of cancer metastasis involves with the dynamic generation and transmission of intracellular, intercellular, and extracellular forces [53-57]. Recently, our group have reported that the cellular force evolution correlates with the metastatic-like dispersion in vitro [58]. The dispersion is both gel stiffness and colony size dependent: it occurs for cell colonies on stiff gels rather than on soft ones; smaller colonies disperse earlier than larger ones. From both the experiments and simulations, we now know that the traction force landscape is colony size and gel stiffness dependent (shown in Figure 3.11), indicating a positive correlation between the traction force landscape and the dispersion behavior.

Applying the biophysical model in the previous chapter, we generate a traction force phase diagram in the parametric space of gel stiffness (2 to 50kPa) and colony size (50 to 250μm radius) from which we identify a traction force threshold criterion that separates the cohesive and dispersive phenotypes observed in experiments, shown in Figure 3.12. The symbols "Δ" and "◯" represent dispersed and non-dispersed colonies, respectively, based on the experimental observations of about 50 colony samples. The contour map stands for the average traction forces in the boundary layer whose width is 50μm. From the overlapping simulation results and

experimental data, one can identify a contour that roughly separates the "Δ" and "◯", which is represented by the dash line. The force threshold is $T_c \approx 125$Pa: a threshold signifies the onset of the metastatic-like dispersion a of HCT-8 cell colonies. Once the average traction forces in the boundary layer reaches T_c, the dispersion of the cell colonies initiates, otherwise the cell colonies remain cohesive. The phase diagram further suggests that at given gel stiffness, smaller colonies have a higher metastatic potential; while at a given colony radius, increasing the gel stiffness would drive the metastatic phenotypic change.

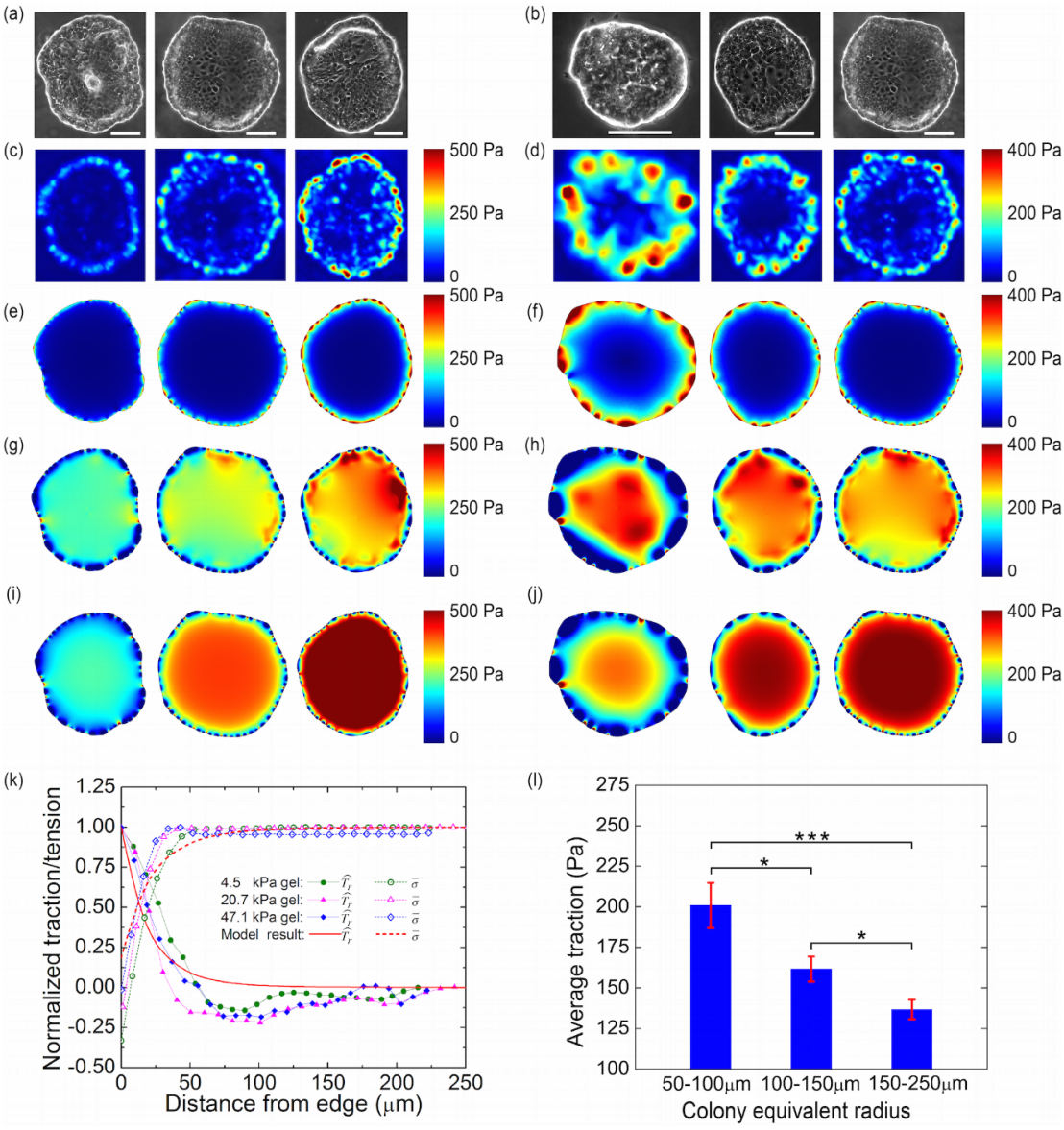

Fig. 3.11. Traction force is both substrate stiffness (Left panel) and colony size (Right panel) dependent. (a-b): Phase contrast images of HCT-8 cell colonies on different gel stiffness (a1,with gel stiffness of 4.5kPa, 20.7kPa and 47.1kPa, respectively; scale bar: 100μm) and with different monolayer sizes (a2, scale bar: 100μm) on 20.7kPa gels. (c-f) The traction force profiles of the cell colonies obtained by TFM (c-d) and modeling (e-f), respectively. (g-j) The intercellular tension maps of the cell colonies obtained by MSM (g-h) and modeling (i-j). (k) Spatial distribution of traction force (solid line) and intercellular tension (dash line), normalized by their maxima, respectively. (l) The average traction force at the boundary layer (the summation of traction force in the region within 50 mm from colony boundary divided by the area of the region).

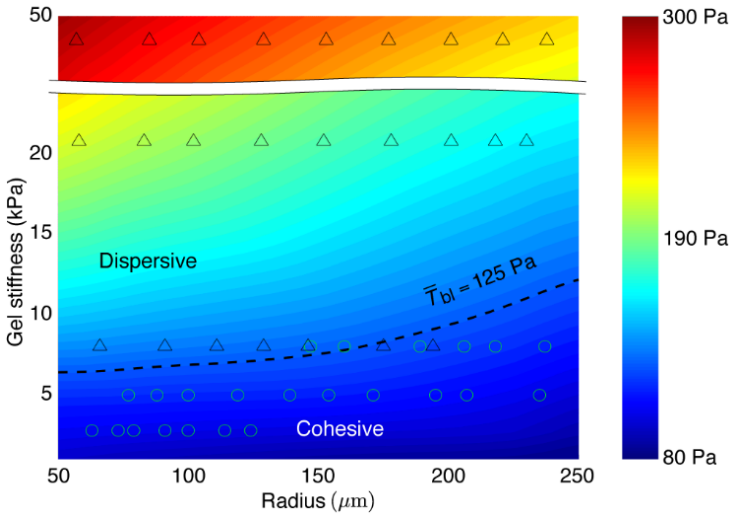

Fig. 3.12. Phase diagram of average traction at the boundary layer in the stiffness-size plane computed by the biophysical model, overlapped with the dispersion behavior of many cell colonies observed in the experiments. The dashed lines represent constant traction contours in the parametric space. A phase boundary of constant traction 125Pa, separating the dispersive and cohesive cell colonies, is identified, representing a force-threshold criterion for the malignant phenotypic change.

3.8. Conclusion and summary

In this chapter, we apply our thermodynamic model to predict the substrate stiffness dependent active contractility for NIH 3T3 cells and HCT-8 colonies. We conclude that cell active stress increases as the substrate stiffness increases, and then reaches a maximum value as the substrate gets stiff enough. We then predict the geometry regulated traction force landscape and focal adhesion profile for single SaOS-2 cells, validated by experiments. The traction forces and the focal adhesions co-localize at the convex boundaries and vanish at the concave boundaries. Next, we present the geometry regulated cellular tension landscape for cells patterned on glass. In this example, we show the advantage of our model compared with TFM. Finally, the reciprocal cell-matrix coupling, the colony size effect, and the substrate stiffness effect of HCT-8 cell colonies are well captured by the model. A traction threshold is identified in the metastatic-like dispersion of HCT-8 cell colonies.

Chapter 4

Phase-field model for the prediction of the distribution of myosin motors and the morphology of stress fibers

4.1. Introduction

In the previous chapters, we developed a microstructure-based thermodynamic model that successfully captures the positive feedback mechanical network in traction force generation and transmission in single cells and multicellular monolayers. However, this model still has some limitations. Firstly, the cell monolayer is assumed to be a piece of thin, homogeneous, and isotropic elastic material. Yet a cell itself is a composite structure made by different materials. For instance, most matters inside a cell is consisted of liquid, which is highly deformable. The actin stress fiber, the most important part to sustain cellular stress, is much stiffer and usually has a Young's modulus in the order of 10^6Pa [59, 60]. Thus, it is not difficult to infer that the cellular modulus is relatively higher at the place where there are more stress fibers. Atomic force microscopy (AFM) has shown that the stiffness of the cell varies as the tested location changes, which may arise from the heterogenous distribution of stress fibers [61-66]. This draws the second limitation of the thermodynamic model: it totally neglects the abundant details of microstructure evolution inside the cell. For example, the binding and unbinding of myosin motors onto stress fibers at different locations inside a cell define the active contractility profile of that cell [67]. A nonuniform active contractility will lead to a different traction force landscape comparing with the uniform active contractility assumption. Thirdly, our thermodynamic model can only predict the statics of cells, while it cannot tell us how the cells reach it. Lacking kinetic details makes our model unable to predict evolutionary processes. A microstructure-based kinetic

model needs to be developed to look deeper into the microstructure evolution inside a cell.

In this chapter, we develop a kinetic model to incorporate the elastic and interfacial effect, as well as the kinetics of myosin motors. Myosins, a family of motor proteins, contribute to the generation of active contractility inside a cell and other motility processes by consuming ATP [24]. The myosin motors are originally freely diffusive molecules inside a cell. Once a mechanosensitive signaling pathway, such as the Rho-ROCK or the MLCK pathway, is open, the myosin motors will respond to it and bind themselves onto the stress fibers and contract them, developing intracellular tension inside the fibers and helping them assemble into cytoskeletons [68, 69]. The cytoskeletons are connected with focal adhesion points in order to transmit the intracellular tensions to substrate. The evolution of myosin motors can be characterized by the evolution of a material phase, which couples with the traction force generation and transmission, and the elasticity of cell monolayer. Therefore, a phase-field model is proposed in this chapter.

Before moving on to the next section, we would like to give a brief introduction on the phase-field model (PFM). The PFM is a powerful tool to simulate the coevolution of the microstructures at mesoscale. The microstructures in PFM are defined by a series of continuous field variables, called the order parameters. These parameters usually range from 0 to 1 or -1 to 1. The evolution of these variables is depicted by a free energy functional. The energy functional with only one phase variable has the simplest form as shown below [70]:

$$F = \int_{\Omega}[\frac{k}{2}(\nabla \mathrm{c})^2 + G(\mathrm{c}) + f(\mathrm{c})]\mathrm{d}\Omega, \tag{4-1}$$

where c is the phase variable. The first term in the integral is the gradient energy, where the parameter k defines the thickness of the phase boundary. Namely, a small value of k gives a sharp

phase boundary, while a large k gives a diffusive phase boundary. The second term is the local free-energy density function, usually represented by a double-wall potential or other polynomial. The last term contains the energy from all kinds of long-range and short-range interactions, such as chemical interactions, elastic interactions, and electrical interactions. The phase variable c can be categorized into two kinds: conserved variables and non-conserved variables. The conserved variables should satisfy the local conservation condition, whose evolution follows Cahn-Hilliard equation. The evolution of the non-conserved variable, on the other hand, follows Allen-Cahn equation.

4.2. Equations

We model the cell as a two-dimensional, active, thin elastic layer with a thickness h, occupying an area A. The cell actively contracts, enabled by myosin motors pulling the actin filaments. Linking the cell and the substrate are the focal adhesion complexes that sustain and transmit traction forces **T**. The free energy of the cell and the focal adhesion is written as:

$$F(c;\rho;\mathbf{u}) = \int_A [\tfrac{k}{2}(\nabla c)^2 + f_{ch}^{c}(c;\mathbf{u}) + f_{el}(c;\mathbf{u}) + f_{ch}^{\rho}(\rho;\mathbf{u})]\mathrm{dA} + \int_{\partial A} \Gamma \mathrm{d}\ell, \quad (4\text{-}2)$$

where **u** is the displacement vector; c is the order parameter that characterizes the density of myosin motors binding to stress fibers, ranging from 0 to 1; ρ is the focal adhesion concentration;; Γ is the line tension acting on the boundary of the cell. The first term in the first integral in Equation (4-2) is the gradient energy; the second term is the chemical energy density of the myosin motors; the third term is the elastic strain energy density in the cell sheet; the fourth term is the chemical energy of the focal adhesions; and the second integral stands for the line energy. Here for simplicity, we assume the displacement in the substrate is so small by comparing with that in the cell so the strain energy it carries can be neglected. We model the myosin as a material phase which is conserved

and can diffuse freely in the cell domain, and use $f_{ch}^{c}(\mathrm{c};\mathbf{u})$ to characterize its energy landscape:

$$f_{ch}^{c}(\mathrm{c};\mathbf{u}) = \Omega c(1-c) + nRT[c\ln c + (1-c)\ln(1-c)] - \alpha(c-c_0)\sigma_1. \quad (4\text{-}3)$$

The first term in Equation (4-3) is the double-well energy function [71], whose profile is controlled by the parameter Ω . The second term stands for the mixture entropy of the myosin-motor-rich phase and the myosin-motor-free phase, where T is the room temperature; R is the ideal gas constant, n is a relative density of c. The last term is the binding energy term, same as the adhesion energy addressed in focal adhesion formations. Upon a cell attaching to a substrate, a few motor proteins "actively" generate contractile strain inside the cell. Once the cell finds that in some regions tension can be established in certain directions, more motor proteins will flow to those regions because the binding energy between the motor proteins and the actin fibers are lower when the fibers are in tension and higher when they are in compression. Here, we hypothesize that the myosin motors are mainly attracted by the first principal stress σ_1. By using σ_1, we note that the motor proteins mainly feel the tension in the direction of σ_1, in which actin fibers align [72]. The parameter c_0 is the reference myosin density, and α characterizes the strength of the binding between motor proteins and stress fibers. The cell is modeled as a thin linear elastic sheet. The elastic strain energy density $f_{el}(c,\boldsymbol{u})$ is written as:

$$f_{el}(c;\mathbf{u}) = \frac{1}{2}h\sigma_{ij}^{el}(c;\mathbf{u})\varepsilon_{ij}^{el}(c;\mathbf{u}), \quad (4\text{-}4)$$

where h is the cell thickness. The elastic stain tensor $\varepsilon_{kl}(c;\mathbf{u})$is:

$$\varepsilon_{ij}^{el}(c;\mathbf{u}) = \varepsilon_{ij}^{tot}(\mathbf{u}) - \varepsilon_{ij}^{c}(c;\mathbf{u}) = \frac{1}{2}\left(u_{i,j} + u_{j,i}\right) + (\varepsilon_0 + \beta c^2)\delta_{ij}, \quad (4\text{-}5)$$

where the term in the first term is the total strain, while the second term is the active contractility of the cell, resembling a thermal cooling. The small parameter ε_0 is used as a perturbation and β is a parameter meaning the active strain increased per myosin density squared. The higher-order term on c shows that the active contractility is sensitive to myosin motors, that is, only a small amount of motors can induce a certain amount of contractility. Based on the previous conclusions,

the active contractility is substrate stiffness dependent, hence ε_0 and β are parameters varying with the substrate stiffness. By applying Hooke's law for plane stress, the stress tensor $\sigma_{ij}^{el}(c;\mathbf{u})$ is written as:

$$\sigma_{ij}^{el}(c;\mathbf{u}) = \frac{E(c)}{1-\nu^2}\left[\nu\,\delta_{ij}\varepsilon_{kk}^{el} + \frac{(1-\nu)}{2}(\varepsilon_{ij}^{el} + \varepsilon_{ji}^{el})\right], \tag{4-6}$$

where Young's modulus E is assumed linear dependent on c: $E = E_0 + ck_c$,with E_0 and k_c being constant. As activated myosin motors are bound with stress fibers, the higher density of the motors means more stress fibers assembly, making the stiffness larger. The chemical energy of focal adhesion $f_{ch}^{\rho}(\rho;\mathbf{u})$ equals to:

$$f_{ch}^{\rho}(\rho;\mathbf{u}) = n_l(\rho\mu_0 + \rho\ln\rho + \frac{1}{2}\rho\zeta|\boldsymbol{u}|^2 - \rho\gamma), \tag{4-7}$$

where n_l is the lattice number on cell membrane. The first term is the energy in reference configuration, where μ_0 is the reference chemical potential. The second term is entropy derived by the ideal solution of gases. The third term is the elastic stretch energy in the ligand-receptor bond. The ligand-receptor bond is modeled as linear springs as what we did in previous chapters. The constant ζ is the spring constant; the approximation $\Delta\mathbf{u} \approx \mathbf{u}$ is used here. Since integrins are force-sensitive and force-responsive molecules, they can feel the extracellular tension and aggregate in response to the existent of it. The last term adhesion energy takes the form $\gamma{\sim}\zeta|\mathbf{u}|^2$. We note that the energy of focal adhesion is calculated in the unit of k_BT, like what we did in Chapter 2. Since we want to focus on the phase evolution on myosin motors and reduce total the computing cost, the evolution of the focal adhesion is not modeled by phase-field method.

The chemical potentials with respect to the myosin and integrin are derived from the partial variation of the free energy functional:

$$\mu_c = -k\nabla^2 c + \Omega(1-2c) + nRT\ln\frac{c}{1-c} + \frac{\partial E(c)/\partial c}{2(1-\nu^2)}h\left[\nu\,\delta_{ij}\varepsilon_{kk}^{el} + \frac{(1-\nu)}{2}\left(\varepsilon_{ij}^{el} + \varepsilon_{ji}^{el}\right)\right]\varepsilon_{kl}^{el}(c;\mathbf{u}) +$$

$$\frac{2\sigma_{kk}c\beta}{1+\nu} - \alpha\sigma_1, \tag{4-8.1}$$

$$\mu_\rho = n_l(\mu_0 + \ln\rho + \frac{1}{2}\zeta|\boldsymbol{u}|^2 - \gamma). \tag{4-8.2}$$

As a molecular whose quantity conserves locally, Cahn-Hilliard equation is adopted to characterize the kinetics of myosin motor evolution:

$$\frac{\partial c}{\partial t} = \nabla \cdot M\nabla\mu_c, \tag{4-9}$$

where *M* is the mobility parameter. The boundary condition is assumed to be:

$$\nabla c \cdot \mathbf{n} = 0, \tag{4-10.1}$$

$$\nabla\mu_c \cdot \mathbf{n} = 0, \tag{4-10.2}$$

where **n** is the outer unit normal of the cell boundary. Since the focal adhesions can be assembled and disassembled, their quantity does not conserve. The kinetics is simply described by Allen-Cahn equation:

$$\frac{\partial \rho}{\partial t} = -L\mu_\rho, \tag{4-11}$$

where *L* is the mobility parameter. The stress equilibrium equation and its boundary condition are derived by minimization the free energy with respect to the displacement **u**:

$$\nabla \cdot \boldsymbol{\sigma} - \zeta\rho\mathbf{u}/h = 0 \text{ in } A, \tag{4-12}$$

$$\boldsymbol{\sigma} \cdot \mathbf{n} = -\frac{\Gamma\kappa}{h}\mathbf{n} \text{ on } \partial A, \tag{4-13}$$

where κ is the curvature **n** and is the outer unit normal of the cell boundary, respectively. The initial conditions for the density of myosin motors and focal adhesions are that they are both uniformly distributed within the cell with a value of c_0 and ρ_0, respectively.

4.3. Numerical implementation

Apply weak form in COMSOL

Due to the nonlinearity of the system, we apply finite elements method to solve the equations. Firstly, we write Equation (4-9) to (4-13) into the weak form:

$$\int_A \{k\nabla c \cdot \nabla \tilde{c} + [(\frac{\delta f_{ch}(c)}{\delta c} + \frac{\delta f_{el}(c;\mathbf{u})}{\delta c}) - \mu_c]\tilde{c}\}\mathrm{dA} = 0, \tag{4-14.1}$$

$$\int_A \{k\nabla \mu_c \cdot \nabla \tilde{\mu}_c + \frac{\partial c}{\partial t}\tilde{\mu}_c\}\mathrm{dA} = 0, \tag{4-14.2}$$

$$\int_A (\mu_\rho + \frac{\partial \rho}{\partial t})\tilde{\mu}_\rho \mathrm{dA} = 0, \tag{4-14.3}$$

$$\int_A [\boldsymbol{\sigma} \cdot (\nabla \tilde{\mathbf{u}})_{sym} + Y\mathbf{u} \cdot \tilde{\mathbf{u}}/h]\mathrm{dA} - \int_{\partial A} (-\Gamma\kappa/h\tilde{\mathbf{u}} \cdot \mathbf{n})\mathrm{d}\ell = 0, \tag{4-14.4}$$

where "~" means test functions. We implement the weak forms into the commercial package COMSOL. A ten-node cubic triangle element is used to generate the mesh, which fulfills the accuracy of the problem. For single cells, the mesh size is $1\sim2\mu\mathrm{m}$. The number of elements is in the order of 10^3; the total number of the degree of the freedom is in the order of 10^4. For cell colonies, the mesh size is around $2.5\sim7.5\mu\mathrm{m}$, as the radius of the colony increases from $50\mu\mathrm{m}$ to $150\mu\mathrm{m}$. The number of elements is still in the order of 10^3; the total number of the degree of the freedom is in the order of 10^4. We adopt the adaptive time step scheme offered by COMSOL for the time integration. To ensure the accuracy of the time integration, the relative tolerance of each time step is set to be 10^{-4}. We use default settings in the solver to solve the equations along with boundary conditions in a fully coupled manner. Parallel computing is used for 20 CPUs. Since we do not solve the equilibrium in the substrate in this section, the total solution time reduces to about 2~3 hours.

Parameter settings

In this section, we will discuss how we choose parameters for our phase-field model. We assume that the parameters in our model are mainly cell-type dependent, meaning the same kind of cell or cell colonies shares roughly the same parameters, just like what we did in Chapter 2. In this section, we firstly give the order of the magnitude of the parameter. The exact values of the parameters are determined by matching our prediction on the traction force landscape with the experiment results of real cells. The values of parameters used for the single cells and cohesive colonies in Section 4.4 are listed in Appendix A.

Firstly, we determine the material parameters and the geometry parameter for the cells. For Young's modulus and Poisson's ratios of cells, previous studies show that they are usually in the range of $10^3 \sim 10^4$Pa and $0.4 \sim 0.5$, respectively [18-20, 40]. Therefore, we set E_0 in the order of magnitude of 10^3Pa and k_c in the order of magnitude of 10^4Pa. Since the normalized density of myosin motors ranges from 0 to 1, the Young's modulus E is in the order of magnitude of 10^3Pa, which conforms with experimental measurements. The parameter ε_0 and β are in the order of 10^{-2} and 10^{-1} so that the deformation is small. The thickness of the cell sheets is directly measured from the experiment, which is in the order of $10^0 \sim 10^1$μm.

Next, we determine the parameters associated with myosin motors. The relative density n is set in the order of 10^{-19}mol/μm^2 so that the lattice number per area of myosin motor is in the order of 10^5/μm^2. The double-well energy function coefficient Ω is in the order of $10^{-16} \sim 10^{-15}$J/μm^2, so that the double-well energy is in comparable with the entropy. The parameter α is in the order of 10^{-7}m to ensure the convergence and reasonable predictions. The coefficient of the

gradient energy k is determined to make the interfaces of different phases to be diffusive. For focal adhesions, the parameter n_l, μ_0, and ζ are determined in the same way with that in Chapter 2 and are in the same order of the magnitude. The line tensions used in this chapter is also adopted from Chapter 2.

4.4 Results and Discussions

Validation of the model: applying it on single cells and multicellular structures.

In this section, we apply the phase-field model onto single fibroblasts and cell colonies to validate its correctness. We will see that the model can fully replicate results in the previous studies. All the model parameters used in this section can be found in Table A.3 in Appendix A.

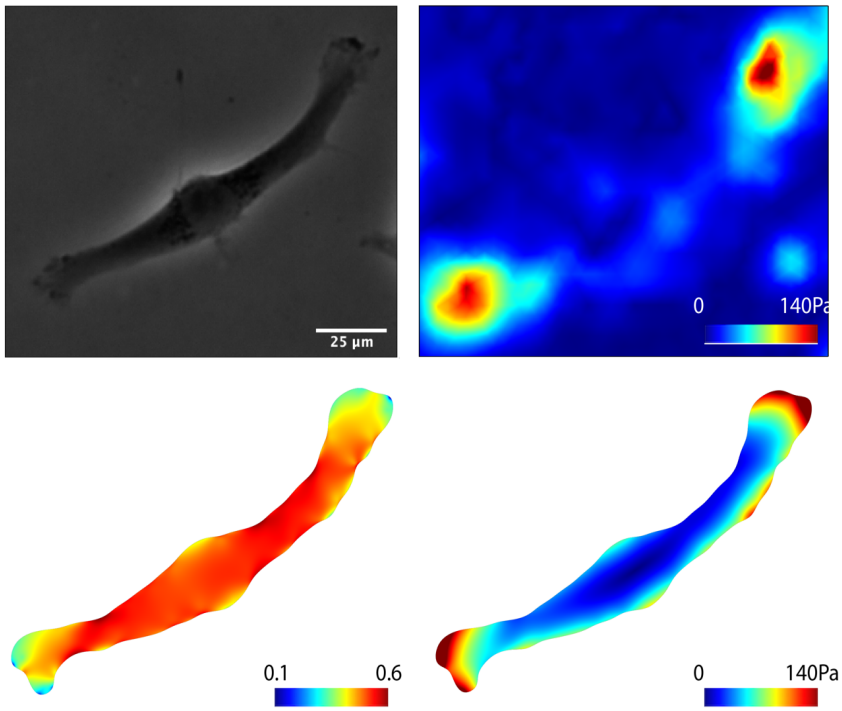

Fig. 4.1. Experimental and simulation results of a single needle-like 3T3 fibroblast: upper left: phase contrast of the cell; upper right: TFM results of the cell; bottom left: the concentration profile of the myosin motors in the cell; bottom right: the predicted traction force landscape.

We firstly apply our phase-field model to a single needle-like fibroblast. By looking into the right column of Figure 4.1, we can see that the traction force predicted by the new kinetic model agrees well with the TFM results. That is, most of the traction forces are highly localized at the two ends of the cell. The predicted myosin motor density shown in the bottom left has an opposite trend to that of the traction forces. It is relatively smaller at the cell ends and then ramps up quickly, reaching a uniform value in the rest area of the cell. This is because the flow of the myosin motors is controlled by the cellular stress as shown in Equation (4-3), and it is not difficult to see that due to the similarity in cell geometries, the landscape of the cellular stress is small at the two cell ends and large in the centroid of the cell.

We then apply the model onto cohesive colonies to see whether it can recover size effect and stiffness effect. The weak form equations (4.14.1) ~ (4.14.3) are solved with respect to cell within the colonies, expect Equation (4.14.4) is solved for the entire colony. As shown in Figure 4.2, perfectly circular colonies are studied. In Figure 4.2 (a), the traction force landscape of colonies with radius of 60μm, 100μm, and 150μm on 40kPa gel (Young's modulus) are plotted. The average traction forces with a 50μm width boundary layers are 188.15Pa, 153.36Pa, and 138.03Pa, respectively. More cases with different colony radius are studied and the average traction forces in boundary layers are calculated. We interpolate the average traction forces with respect to the colony radius and plot the interpolated curve in Figure 4.2 (c) left. The result successfully recovers the size effect of cohesive colonies: the smaller the size, the larger the

average traction forces. We then study colonies with the same radius adhering on substrate with different stiffness. Colonies with a 150μm radius are examined; the traction force landscape of colonies on 6kPa, 20kPa, and 40kPa gels are plotted in Figure 4.2 (b). The parameters in Equation (4-5) are tuned with respect to different gel stiffness, listed in Table A.3 in Appendix. By looking into Figure 4.2 (b), one can see that the magnitude of the traction forces dramatically increases from left to right as the gel stiffness increases. The average traction force in boundary layer reflects the same fact as shown in Figure 4.2 (c) right: the curve is monotonically increasing as the gel Young's modulus increases. Specifically, for colonies on substrate whose stiffness is 6kPa, 20kPa, and 40kPa, the average traction force in the 50μm width boundary layer is 86.81Pa, 112.41Pa, and 138.03Pa, respectively.

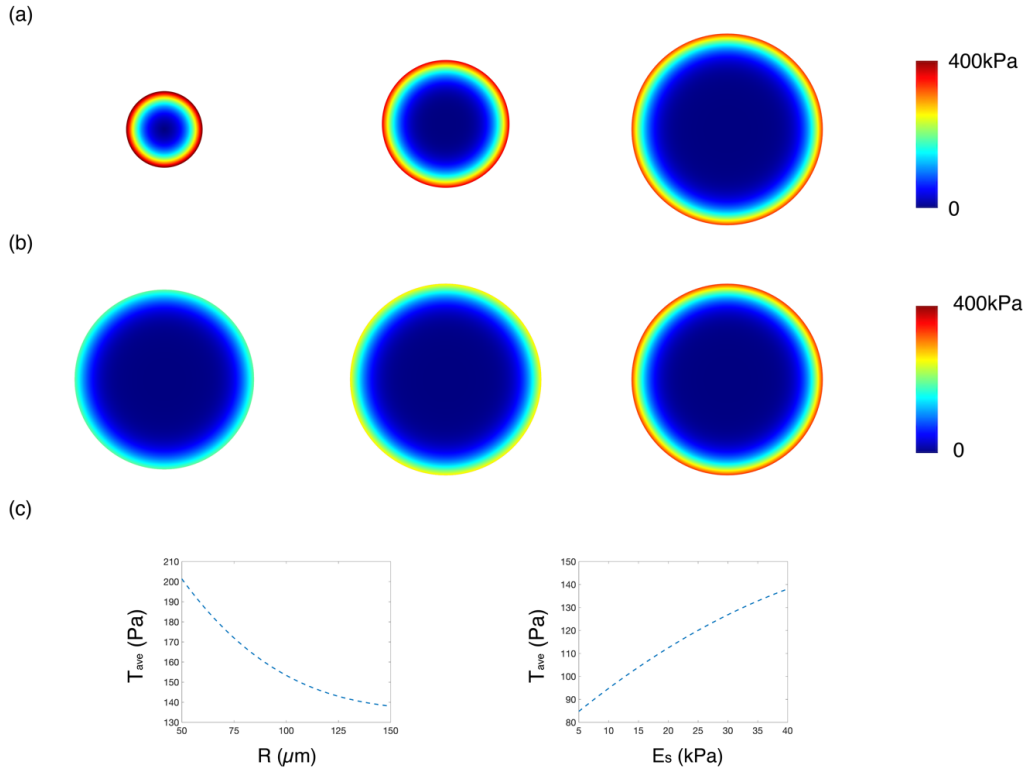

Fig. 4.2. Validation of the size and stiffness effect by the new model. (a) Traction force landscapes of cohesive colonies with radius 60μm, 100μm, and 150μm on 40kPa gel. (b)Traction force landscapes of colonies with a 150μm radius on substrates with Young's

modulus of 6kPa, 20kPa, and 40kPa. (c)Left: average traction force in boundary layer versus colony radius on 20kPa gels; right: average traction force in boundary layer versus gel Young's modulus for colonies with the same radius

We next apply our model to study a previous examined observation: cadherin-based junctions regulate cell-matrix traction forces [73]. Within a multicellular structure, the intercellular forces are transmitted between cells mainly through cell-cell junctions, which are formed by cadherin-based molecules [74]. Recent studies have revealed that the cadherin-based junctions play important roles in some biophysical processes of cells. For instance, strong cell-cell junctions coordinate the mechanical behavior over a large length scale [75]; they also contribute to the metastatic potential [76]; they even can affect the surface tension of cellular aggregation, spreading and migration [77]. Additionally, cadherin-based cell-cell junctions can pose an impact on cell-substrate interactions: experiments show that they are able to rearrange the traction forces [78, 79]. Here we adopt a triple-cell colony system and model the cadherin-based cell-cell junctions as a series of linear springs with a spring constant k_c, the value of which is used to denote the strength of cell-cell junctions. The numerical results are presented in Figure 4.3 (b) and (c): from the left to the right, the strength of the cadherin-based cell-cell junctions monotonically increase. We find that, as the cell-cell junction strength increases, the magnitude of the maximal traction force increases from 70Pa to 120Pa, and the traction force gradually disappears in the intercellular region and re-localizes at the periphery, which coincides with previous studies. It is clearer to see the phenomena happens by looking into the average traction force profile as function of Δ： the distance to the colony centroid, shown in Figure 4.3 (c). The average traction force decreases from 40Pa to 0 as the parameter k_c increases. Such phenomenon happens because the softer cell-cell junctions can deform more than the stiffer ones. As each cell

contracts, more displacement is generated in the soft cell-cell junctions than in the stiff ones. Traction forces are going to generate near the cell-cell junctions since they are proportional to the displacement ($|T| \sim |\mathbf{u}|$). In summary, our model captures the spatial re-organization of traction force landscape owing to the change of intercellular adhesion strength. For strong cell-cell interaction (large k_c), the colony behaves cohesive and deform as an entity, with traction force only appears at the periphery; for weak cell-cell interaction (small k_c), the cells tend to deform individually, with significant traction forces generating near the cell-cell boundaries.

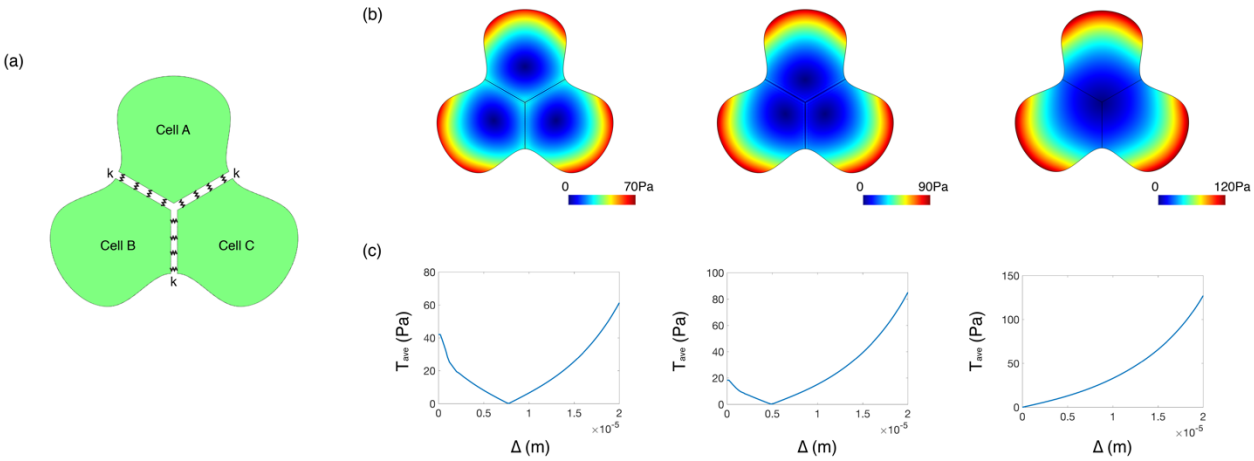

Fig. 4.3. Our model captures cadherin-dependent organization of traction stresses. (a) Schematic of planar colony of three cells, the cell-cell junctions are modeled as a series of linear springs. (b) The traction force landscape versus different cell-cell junction strength. (c) Spatial profiles of average strain traction force as a function of distance, from colony edge for different cell-cell junction strength.

Knot-like morphology of stress fibers in strip-like cells on alternatively coated substrate. The surface properties of substrate play important roles in cell-substrate interactions: they can greatly affect cell migration, differentiation, and growth on substrates [80-82]. Previous studies

show that at least four types of surface properties acting upon cell-substrate interactions, including the amount of charges on the surface, the wettability of the surface, the presence of the chemical functionalities and the adsorption of peptides and proteins of the surface [83]. Substrates whose surfaces are heterogeneously coated with a mixture of the above properties have been made to obtain desired behaviors of cells [84]. For instance, people have developed substrates with heterogeneous polystyrene surfaces composed of oxygen plasma-treated stripes (PSox) with a low hydrophobicity separated by non-treated areas (PS) to guide the orientation of neural cell growth [85]. In this section, we study the actin node formation and the knot-like stress fiber assembly in strip-shape cells patterned on substate whose surface is alternatively coated with fibronectin blocks. As shown in Figure 4.4 (a), fibronectins are coated in the adhesion blocks represented by blue rectangles, where cell integrins can bind with ligands and transmit traction forces. In the gap region represented by blank, the substrate surface is not coated with fibronectins, where cell integrins cannot bind with ligands.

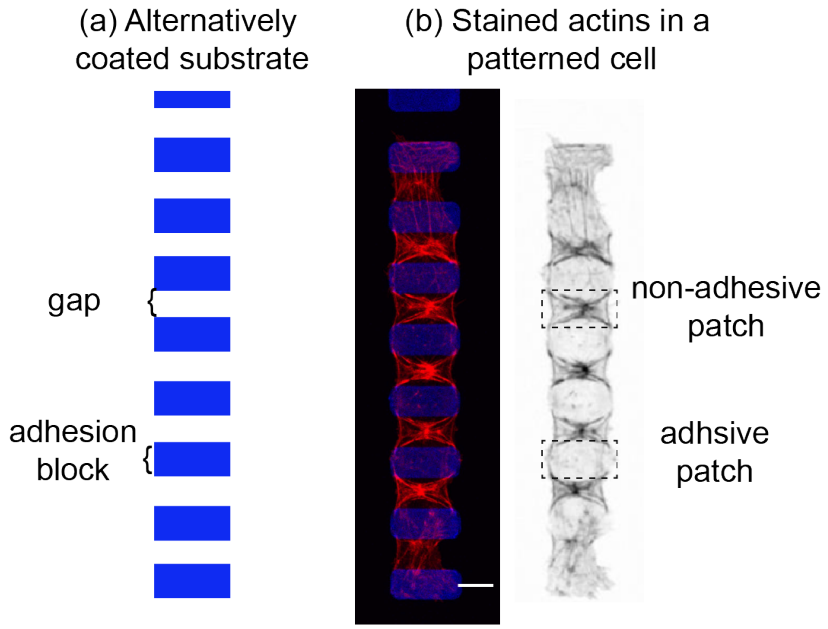

Fig 4.4. The knot-like stress fiber formation in strip-shape cells patterned on substate with heterogeneous surface. (a) The surface of the substrate is alternatively coated with fibronectin in

rectangular blocks (the blue part), while the gap has no fibronectin coated. (b) Stained actins show inhomogeneity of actin node formation and stress fiber assembly in a patterned cell. Actin nodes form in the non-adhesive patches of the cell and vanish in the non-adhesive patches of the cell.

Now we culture the cell onto the substrate and stain its actin filaments. By looking into the experimental results shown in Figure 4.4 (b), we can see that the actins only appear and form into nodes in the non-adhesive patches of the cell, indicating the active contractility is inhomogeneous. We propose that such inhomogeneity is caused by the alternative coating of the substrate surface, which brings a difference between the cell-gap interfacial tension and the cell-adhesion block interfacial tension. Here, we imagine a cell on a substrate whose surface is homogeneous and without coating any fibronectin, and we call the energy stored in the cell-substrate interface as E_0. Now we make the fibronectin coated on some parts of the gel surface to form the pattern in Figure 4.4 (a), and call the energy stored in the interface in this configuration as E_1. We then define the interfacial energy change between these two configurations, that is $\Delta E_{\mathrm{int}} = E_1 - E_0$. One can see that ΔE_{int} arises from two newly created interfaces: the interface between the cell and the coated fibronectins, and the interface between the gel and the coated fibronectins, as shown in Figure 4.5. Therefore, ΔE_{int} is written as:

$$\Delta E_{\mathrm{int}} = \int_{\Omega_{cf}} \Gamma_{cf} \mathrm{d}\,\Omega_{cf} + \int_{\Omega_{gf}} (\Gamma_{gf} - \Gamma_{cg}) \mathrm{d}\,\Omega_{gf}, \tag{4-15}$$

where Ω_{cf} denotes the interface between the cell and the coated fibronectin, with Γ_{cf} being the energy density per unit area stored in the interface; Ω_{gf} denotes the interface between the gel and the fibronectin, with Γ_{gf} being the energy density per unit area stored in it; Γ_{cg} is the energy density per unit area stored in the cell-gel interface.

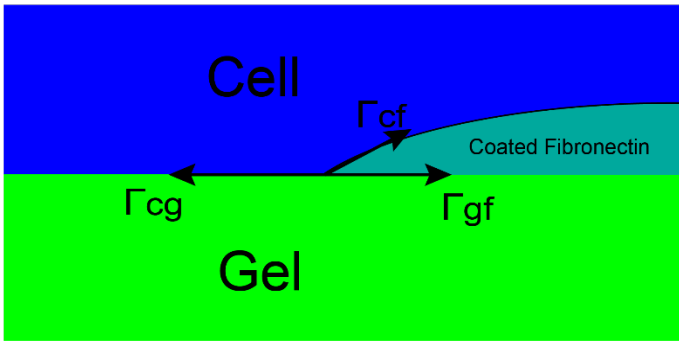

Fig 4.5. The illustration of the interfaces after the gel surface is partially coated with fibronectin. Here three surface tension: Γ_{cf}, Γ_{cg}, and Γ_{gf} form the Neumann triangle.

One should notice that only the variation of first term in in Equation (4-15) with respect to the cell displacement leads to a non-zero result (assuming that cell can only displace the substrate little and the fibronectin coating is fixed on gel) and it is:

$$\delta \Delta E_{\text{int}} / \delta \mathbf{u} = \Gamma_{cf} \int_{\Omega_{cf}} \kappa_1 \mathbf{n} \mathrm{d}\, \Omega_{cf}, \tag{4-16}$$

where κ_1 is the first principal curvature of the interface between the cell and the coated fibronectin, and $\mathbf{n}$ is the unit normal of the interface, pointing toward to the substrate. By assuming that the curvature is localized near the boundary between the cell-gel interface and the cell-fibronectin interface, the tangential component of the right-hand-side of Equation (4-16) leads to an effective line force $\Delta\Gamma$ acting on the boundary between the adhesive patch and the non-adhesive patch of the cell. This line force $\Delta\Gamma$ compresses the adhesive patches, preventing the assembly of actin filaments in this region, while it pulls the non-adhesive patches along the cell longitude direction to initiate the actin filaments assembly only in this part of the cell, not elsewhere. Meanwhile, the line tension generates effective pulling forces in the cell width direction at both sides of the cell. The two forces, together, lead to the focal adhesion formation in the corners of the adhesion patches and the traction force generation in the diagonals of the

non-adhesive patches. Owing to the traction forces in the diagonal directions, stress fibers assemble into the knot-like morphology and the actin node forms in the non-adhesive patches.

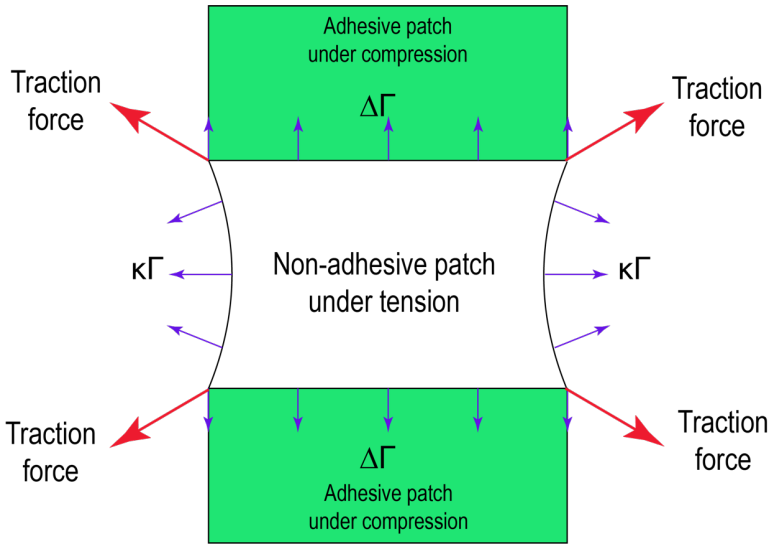

Fig. 4.6. Physical process happened in the cell on alternatively coated substrate. The purple arrows on the top and bottom boundaries of the non-adhesive patch denote for the effective line force ΔΓ led by the difference in the interfacial tensions. The purple arrows on the left and right boundaries of the non-adhesive patch denote for the effective pulling force led by the line tension. Red arrows stand for the traction forces.

We first apply our model to simulate the morphology of stress fibers for cells with different gap sizes on substrate with the same stiffness. For simplicity, we only model one period of the long strip cell and apply periodic boundary conditions on the top and bottom boundaries. The myosin motors and focal adhesions are initially uniformly distributed in the non-adhesive patches and the adhesive patches with densities equal to c_0 and ρ_0, respectively. The model parameters can be found in Table A.4 in Appendix A. The experimental results on 10.6kPa gel are plotted in Figure 4.7 (a), while the simulation results are plotted in Figure 4.7 (b). For the simulation results, we plot the magnitude and the direction of the first principal stress by color contours and

arrows. They are used to represent the density of actin filaments and the direction of stress fibers, respectively [72]. For the gap sizes larger than 4μm, actin mode formations are observed in the experiment. Our prediction agrees well with the experiment: for the gap sizes equal to 6, 8, and 10μm, stress fibers assemble into knot-like configurations in the central region of non-adhesive patches. As the gap size decreases to 4μm, the actin node formation fails. Instead, the stress fibers tend to align in the cell width direction, shown by the experiment. This is because the flat geometry of the gap tends to regulate the traction forces to be parallel to the boundaries between the adhesive and non-adhesive patches. Our prediction captures the failure of the actin node formation for 4μm gaps as well. For the case where no gap is made on the surface of the substrate, the traction forces are localized in the two ends of the cell, thus stress fibers are aligned in the longitude direction of the cell.

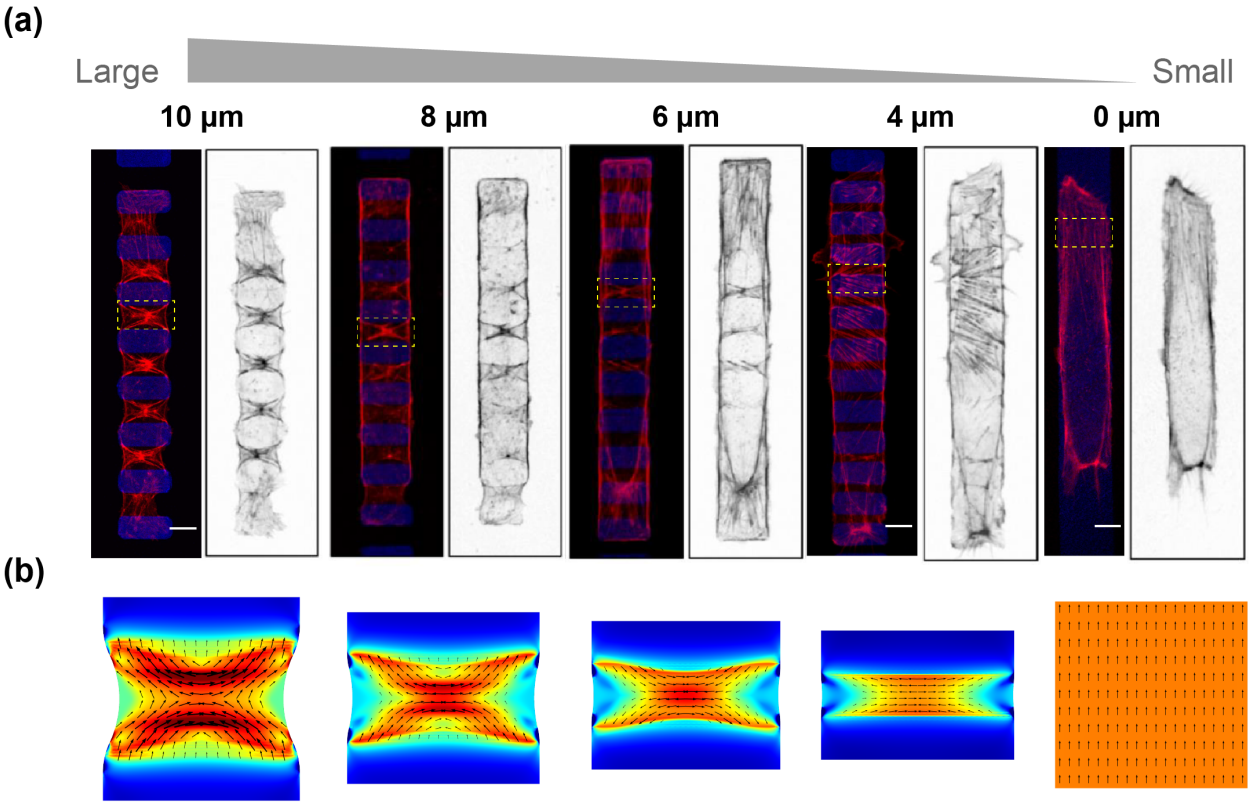

Fig 4.7. Morphology of stress fibers with respect to different gap size on 10.6kPa gel. (a)

Experimental results on stress fiber formation. Pictures have been taken with respect to different gap size. Actin fiber is extracted from the pictures for each case and plotted aside. (b) Simulation of stress fiber formation denoted by the first principal stress σ_1. Colors stand for magnitude of σ_1 and arrows stand for the direction. Red means large and blue means small.

By looking into the magnitudes of the first principal stress σ_1 for different gap sizes, one can see that they mainly concentrate in the diagonals and the centroids of the non-adhesive patches of the cells. As the gap size decreases, the magnitudes of the first principal stress also decreases. For the case where there is no gap, a uniform contractility spans over the most part of the cell.

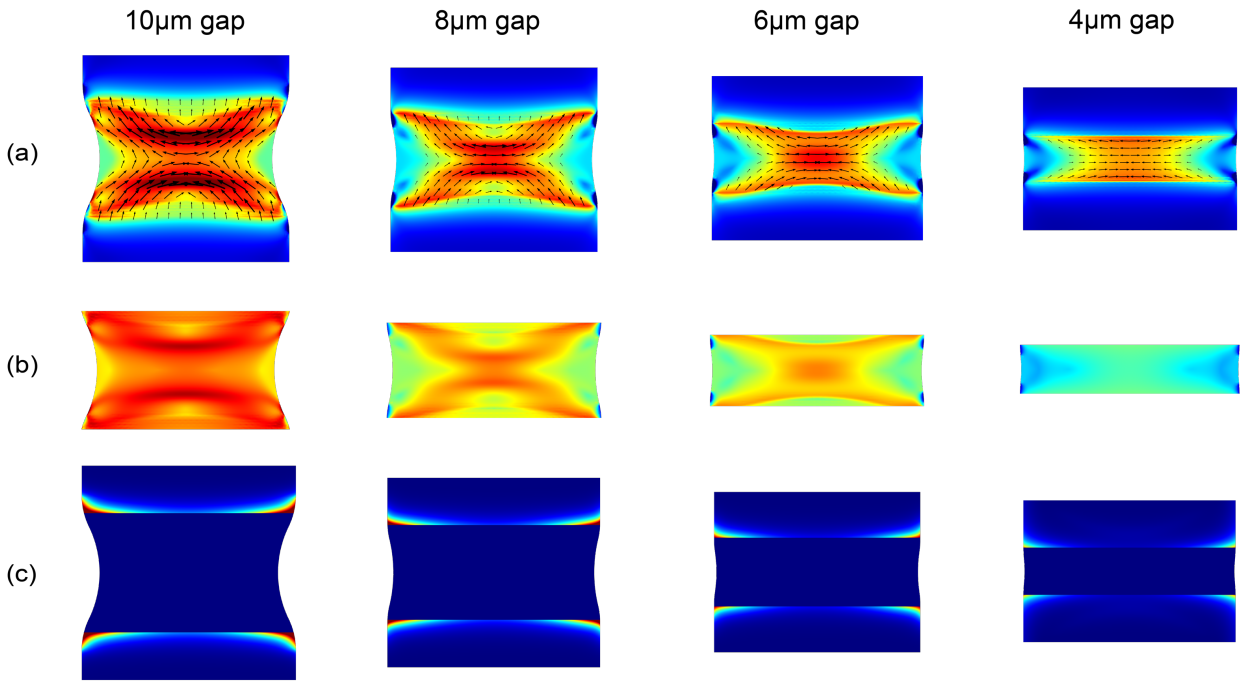

Fig. 4.8. The simulation results on the first principal stress (a) and myosin motor density (b) and focal adhesion concentration (c) with respect to different gap sizes. Red means large and blue means small.

The myosin motor density and the focal adhesion distribution are shown in Figure 4.8 (b) and (c), respectively. As one can see, the distribution of myosin motors is totally first-principal-

stress-controlled. That is, they concentrate at the place where the first principal stress is large. The focal adhesions, on the other hand, are highly localized in the four corners of the adhesive patch.

We next examine the morphology of stress fibers for a certain gap size with different substrate stiffness. As shown in Figure 4.9 (a), experimental results for cells with 4μm gap size, adhering on 2.8kPa, 7.4kPa, 10.6kPa, 16.7kPa, and 34.9kPa gels, are plotted. For cells on the substrate whose Young's modulus is smaller than 7.4kPa, the active contractility is small and is comparable with the interfacial tension ΔΓ. On one hand, the cellular contractility wants the stress fibers to be assembled in the cell width direction due to the flat geometry of the gap. On the other hand, the interfacial tension ΔΓ wants to steer the stress fibers to be in the cell longitude direction. As a result of the competition between the two factors, the actin nodes form in some non-adhesive patches, which is captured by our simulations and experiments. As the gel stiffness increases, the active contractility increases, which makes the stress fibers align in the cell width direction and actin nodes disappear. For cells on substrate whose Young's modulus is larger than 16.7kPa, the cells form long and straight fibers, starting from one end to the other. This is because as substrate stiffness increases, the cellular contractility increases, and it eventually overwhelms the interfacial tension and hence erases the inhomogeneity in cellular contractility. Under this circumstance, the interfacial tension imposes little effect on the cell and the stress fibers assemble into the same configuration with the cells on the substrate without gaps.

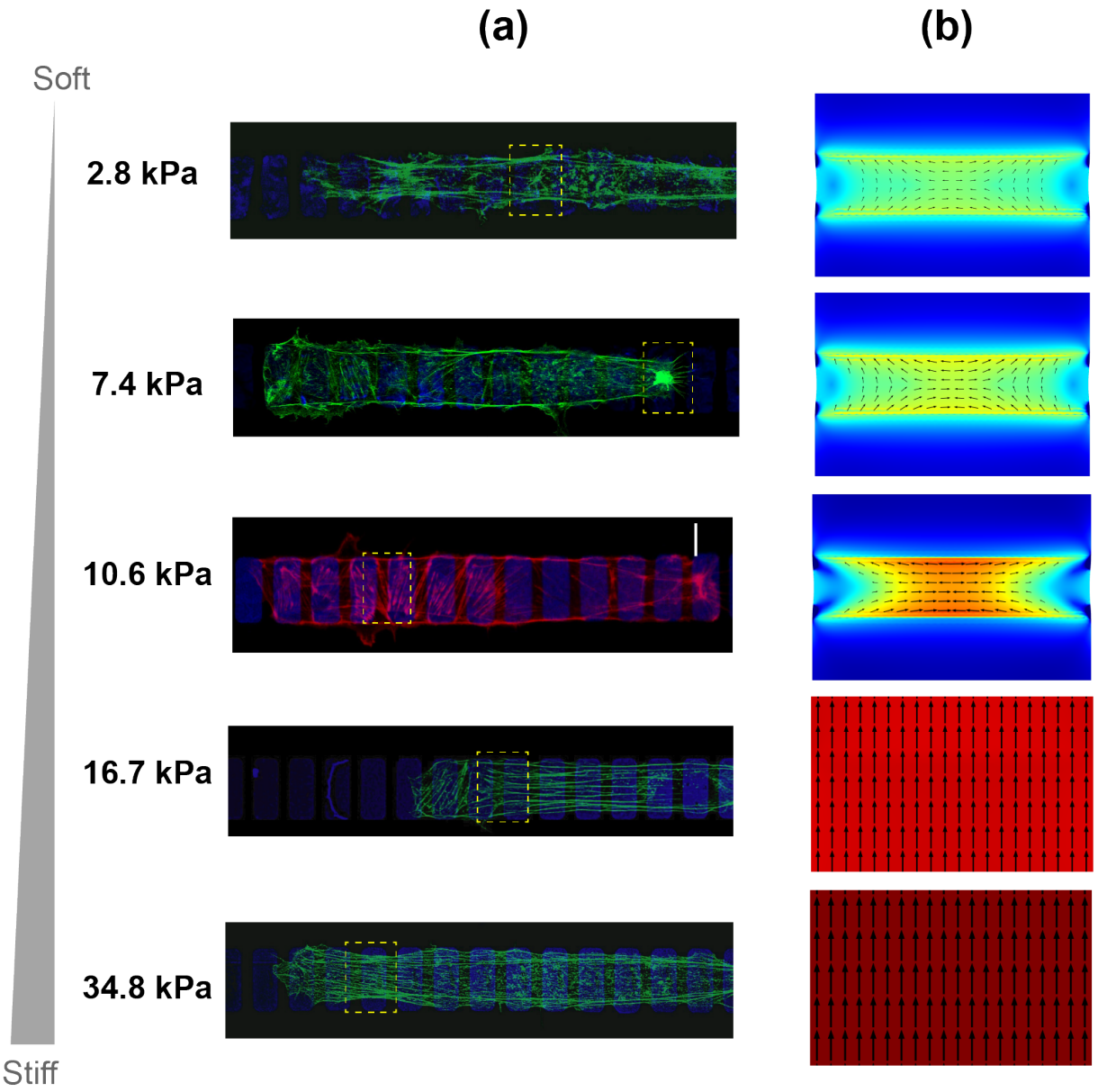

Fig. 4.9. Cells with 4μm gap size on gels with different stiffness. (a) Experimental results on stress fiber configuration 2.8kPa, 7.4kPa, 10.6kPa, 16.7kPa, and 34.9kPa gels (b) Predicted stress fiber direction, denoted by the direction of the first principal stress σ_1, are shown by arrow, whose length is proportional to the average of σ_1.The color contour map represents the magnitude of σ_1.

The conclusion is similar for the 10μm gap case. The difference is that on 2.8kPa gel, the cell fails to form stress fibers as it cannot establish enough contractility to overcome such a large gap

size. By comparing the 2.8kPa results in Figure 4.9 (b) and Figure 4.10 (b), one can see that the magnitude of the first principal stress of 10μm gap case is smaller for that of 4μm gap case, which agrees with the experimental observations.

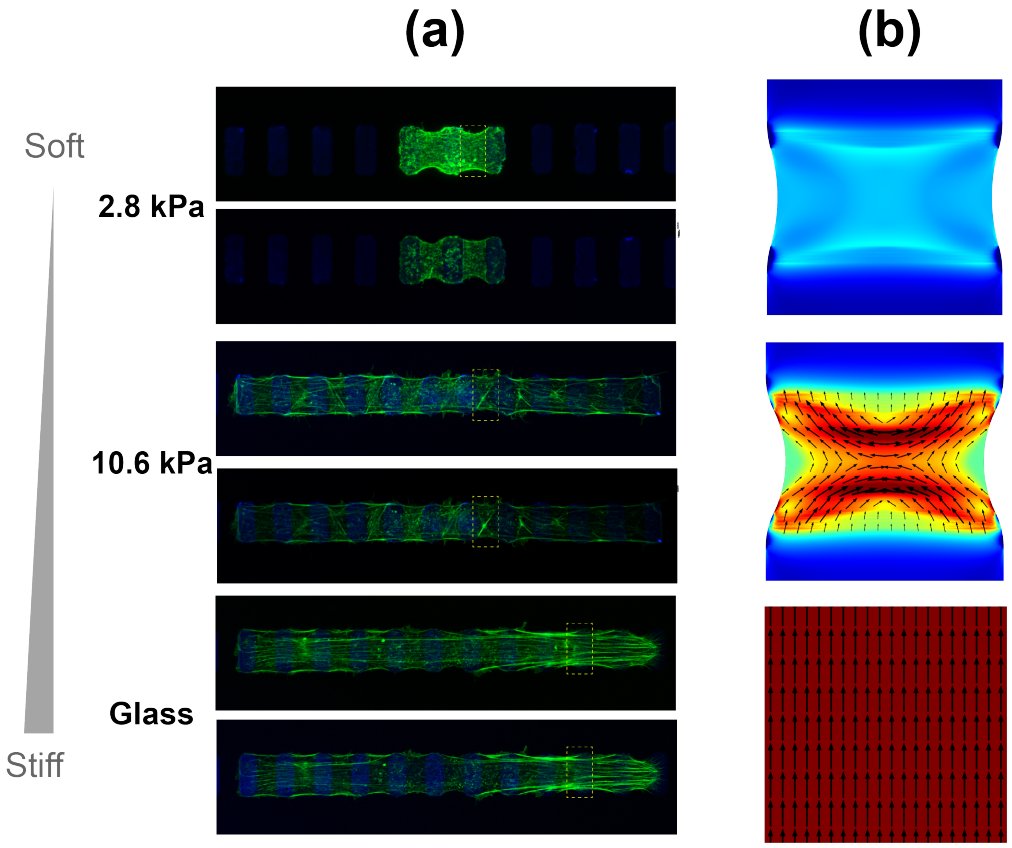

Fig. 4.10. Cells with 10μm gap size on gels with different stiffness. (a) Experimental results on stress fiber configuration 2.8kPa gel, 10.6kPa gels, ands glass (b) Predicted stress fiber direction, denoted by the direction of the first principal stress σ_1, are shown by arrow, whose length is proportional to the average of σ_1.The color contour map represents the magnitude of σ_1.

Next, we continue using our model to predict the configuration of stress fibers for gap sizes equal to 6μm, 8μm, and 10μm. The predictions are plotted in Figure 4.11, where row (a) is for cells on 2.8kPa gel; row (b) is for cells on 7.4kPa gel; row (c) is for cells on 10.6kPa gel; row (d) is for cells on 16.7kPa gel; row (e) is for cells on glass. For cells on 2.8kPa gel, the cellular

contractility is at its minimal, thus stress fiber is hardly formed in this case. As the gel stiffness increases to 7.4kPa, stress fibers start to assemble. The tendency of the actin node formation is quite clear at this moment. With the gel stiffness continuing increasing, we can see clear knot-like configurations of stress fiber assembly in the center of the non-adhesive patches, indicating that the actin node will form in these cases. And there are more and more stress fibers aligning in the cell longitude direction near the top and the bottom of non-adhesive patches as the substrate stiffness increases. Such phenomenon is much more obvious for the larger gaps (8μm & 10μm) than the smaller ones (6μm). Once the substrate becomes rigid, the increasing cell contractility overwhelms the interfacial tension and makes the stress fibers align in the cell longitude direction with their density reaching the maximum. By summarizing the results we obtain, we conclude that the actin node formation succeeds based on three conditions: firstly, the first principal stress should be large enough; secondly, the overall directions of the stress fibers should be in a proper range; thirdly, the stress fibers should not align with each other. Hence, we define three variables to describe whether the actin node formation succeeds. One is the stress-related variable: $\bar{\sigma} = \int_A \sigma_1 \mathrm{dA} \,/\, \int_A \mathrm{dA}$; the other two are direction-related: $\bar{n} = \int_A \mathrm{n}_1^2 \mathrm{dA} \,/\, \int_A \mathrm{dA}$, and $\Delta n = \int_A (n_1^2 - \bar{n})^2 \mathrm{dA} / \int_A \mathrm{dA}$, where n_1 is the horizontal-component of the direction of the first principle stress. The actin node forms only when $\bar{\sigma} > \sigma_c$, $n_c^l < \bar{n} < n_c^u$, and $\Delta n > \Delta n_c$, where σ_c, n_c^1, n_c^2, and Δn_c are all threshold values to determine whether an actin node is formed. The three phase diagrams on $\bar{\sigma}$, $\bar{n}$, and Δn in the parametric space of the gel stiffness and the gap size are presented in Appendix B.

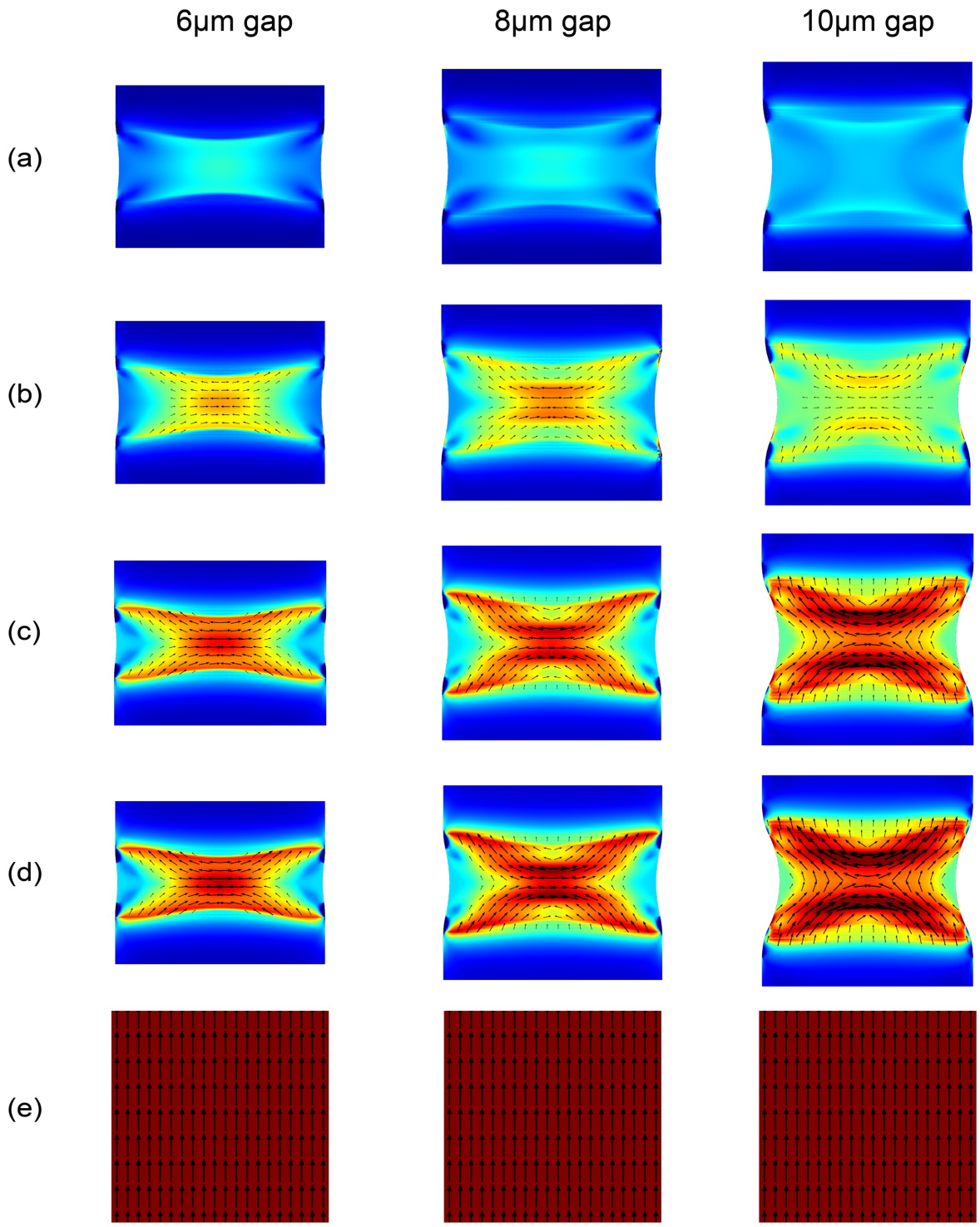

Fig. 4.11. The stress fiber configuration of cells with 6μm, 8μm 10μm gap size on gels with different stiffness. (a) 2.8kPa gel; (b) 7.4kPa gel; (c) 10.6kPa gel; (d) 16.7kPa gel; (e) Glass. The predicted stress fiber direction is denoted by the direction of the first principal stress σ_1, are shown by arrow, whose length is proportional to the average of σ_1.The color contour map

represents the magnitude of σ_1, which is used to represent the stress fiber density.

With the predictions we have made, we can obtain a phase diagram on the actin node formation, which lives in the parametric space of the gap size and the gel stiffness. The phase boundaries are together defined by $\bar{\sigma} = \sigma_c$, $\bar{n} = n_c^u$, $\bar{n} = n_c^l$, and $\Delta n = \Delta n_c$, where $\sigma_c = 70$Pa, $n_c^u = 0.7$, $n_c^l = 0.3$, and $\Delta n_c = 0.14$. For the gap size smaller than 2.5μm, the knot-like stress fiber morphology can hardly form due to the flat geometry of the gap. For cells adhering on gels with stiffness larger than 25kPa, the stress fibers align in the longitude direction of the cells because of the high contractility. For cells adhering on soft substrate with gap size larger than 6μm, the stress fibers fail to form again as there is not enough contractility to bridge such a large non-adhesive patch inside the cell.

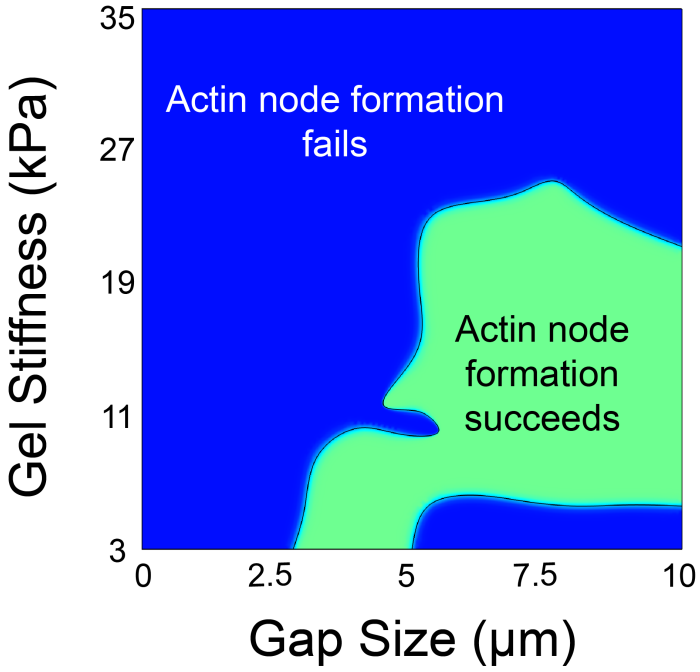

Fig. 4.12. The phase diagram on actin node formation. The horizontal axis is for the gap size, while the perpendicular axis is for the gel stiffness. In the green region, actin node is formed, yet in the blue region, actin node formation fails.

4.5 Conclusion and summary

In this chapter, we have developed a phase-field model on the kinetics of myosin motors, and we also incorporate the evolution of focal adhesions, the elasticity, and the interfacial effect of the cell into the model. The equations and boundary conditions are formulated, and then are implemented by finite elements method. The model is firstly applied onto single fibroblasts and cell colonies to verify its correctness. Its fully replicate results in previous studies, including the size and the stiffness effect, as well as the cadherin-based traction forces. Next, we apply the model on the simulation of the actin node formation in strip-shape cells patterned on substate whose surface is alternatively coated with a fibronectin block. The effect brought by the interfacial tension is addressed. The simulation results agree well with experiments. At last, we come up with a phase diagram on acting node formation with respect to the substrate stiffness and the gap size.

Chapter 5

Conclusions

In this dissertation, we firstly make a review on previous studies on cell-substrate interactions in the Chapter 1. We summarize what has been done by these studies and what needs to be done. Based on the summarization, we come up with a thermodynamic model, considering the elastic effect, edge effect and chemical effect. We apply this model to study single cells and then extend it to multicellular structures. We use this model to predict the active contractility on substrate with different stiffness and find the active stress varies with substrate stiffness. We also find our model successfully predicting the traction force landscape and the focal adhesion distribution for single cells. For cohesive colonies, the model captures the active, nonlinear cell-matrix coupling. It predicts monolayer size and substrate stiffness dependent traction force and intercellular tension, validated by microscopy and immunofluorescence studies. It is suggested that substrate stiffness and colony size can define the efficiency that how cellular tension and cell body stress can be generated. For extremely compliant or stiff substrates and extremely small and large size, abnormally low or high intercellular tension causes the disruption of stress homeostasis, resulting in apoptosis or phenotypic changes, such as metastasis-like cell dispersion.

In chapter 4, a phase-field model incorporating the elastic effect, interfacial effect, and the kinetics of myosin motors is established. The correctness of the model is validated by replicating results in previous studies, such as the size effect and the stiffness effect of cohesive colonies. Strip-like cells on substrate with alternatively coated surface are studied. The model predicts the actin node formation and knot-like morphologies of stress fibers in these cells with the proper

gap sizes and gel stiffness. The results agree well with experiments. We note that the interfacial tension plays an important role in this case.

Appendix A
Model parameters used in the dissertation

We list all the parameters we used in the dissertation in separated tables in this part.

Parameter	Physical Meaning	SaOS-2	NIH 3T3
E	Yong's modulus of cell sheet	5 kPa	5.4 kPa
ν	Poisson's ratio of cell sheet	0.43	0.43
$\hat{\nu}$	Poisson's ration of Substrate	0.48	0.48
σ_A	Active stress: strength of cell contractility	290/360/490 Pa (4/10/20 kPa gel)	See Fig. 3.1
Γ	Line tension	3.67 nN	3.67 nN
h	Thickness of cell sheet	4 μm	3 μm
n_l	Lattice sites per unit area	78000 μm^{-2}	80500μm^{-2}
k	Spring constant of a ligand-receptor bond	16 $k_B T/\mu m^2$	24 $k_B T/\mu m^2$
$\phi_{i,0}$	Fraction of total receptors in i-th cell	0.04	0.08
β	Coefficient of the gradient energy	$5 \times 10^3 k_B T \cdot \mu m^2$	$5 \times 10^3 k_B T \cdot \mu m^2$
$\Delta\mu^0$	Difference of the reference chemical potentials of the bound and free receptors	5 $k_B T$	5 $k_B T$
T	Temperature	300 K	300 K

Tab. A.1. Model parameter used for single SaOs-2 cells and patterned NIH 3T3 cells in Chapter 2 and 3.

Parameter	Physical Meaning	Numerical Value
E	Yong's modulus of cell sheet	10 kPa
ν	Poisson's ratio of cell sheet	0.4
$\hat{\nu}$	Poisson's ration of Substrate	0.47
σ_A	Active stress: strength of cell contractility	330/430/530 Pa (4.5/20.7/47.1 kPa gel)
Γ	Line tension	$2.25/10^7$ N
h	Thickness of cell sheet	12.5 μm
n_l	Lattice sites per unit area	$80500\mu m^{-2}$
k	Spring constant of a ligand-receptor bond	$7.5\ k_BT/\mu m^2$
$\phi_{i,0}$	Fraction of total receptors in *i*-th cell	0.1, with a 2.5% standard error
β	Coefficient of the gradient energy	$1.6 \times 10^4\ k_BT \cdot \mu m^2$
$\Delta\mu^0$	Difference of the reference chemical potentials of the bound and free receptors	$4.5\ k_BT$
T	Temperature	300 K

Tab. A.2. Model parameter used for HCT-8 cohesive colonies in Chapter 2 and 3.

Parameter	Physical Meaning	NIH 3T3/Non-cohesive colony	Cohesive colony
E_0	Initial Yong's modulus of cell sheet	1 kPa	5 kPa
ν	Poisson's ratio of cell sheet	0.43	0.4
k_c	Strengthening coefficient for cell stiffness	9 kPa	7 kPa
ε_0	Contractility perturbation	0.05	0.006/0.008/0.01

β	Strengthening coefficient for cell contractility	0.09	0.042/0.056/0.07
h	Thickness of cell sheet	4 μm *	12.5 μm
n_l	Lattice sites per unit area for focal adhesion	80500 μm^{-2}	80500 μm^{-2}
ζ	Spring constant of a ligand-receptor bond	24 $k_B T/\mu m^2$	9.375 $k_B T/\mu m^2$
μ_0	Chemical potential of receptors in the reference config.	5 $k_B T$	4.5 $k_B T$
k	Coefficient of the gradient energy	40 nJ · μm^2	40 nJ · μm^2
Ω	Coefficient for double-well energy function	1.05×10^{-3} pJ $/\mu m^2$	4.375×10^{-3} pJ$/\mu m^2$
T	Temperature	300 K	300 K
n	a relative density of myosin motors	18100 μm^{-2}	18100 μm^{-2}
α	Coefficient for tension-driving myosin flow	0.8 μm	2.5 μm
c_0	Initial myosin density	0.51	0.5
Γ	Line tension	3.67 nN	$2.25/10^7$ N

Tab. A.3. Model parameter used for the validation part of Section 4.4.

* The thickness of the needle-like NIH 3T3 cell is measured slightly differently from previous papers.

Parameter	Physical Meaning	Patterned strip-like cell
E_0	Initial Yong's modulus of cell sheet	1 kPa

ν	Poisson's ratio of cell sheet	0.43
k_c	Strengthening coefficient for cell stiffness	24 kPa
ε_0	Contractility perturbation	0.024/0.032/0.04/0.043/0.05
β	Strengthening coefficient for cell contractility	0.144/0.192/0.24/0.252/0.3
h	Thickness of cell sheet	4 μm
n_l	Lattice sites per unit area for focal adhesion	$2.65 \times 10^5\ \mu m^{-2}$
ζ	Spring constant of a ligand-receptor bond	$27.2\ k_B T/\mu m^2$
μ_0	Chemical potential of receptors in the reference config.	$5\ k_B T$
k	Coefficient of the gradient energy	$40\ nJ \cdot \mu m^2$
Ω	Coefficient for double-well energy function	$1.45 \times 10^{-3}\ pJ/\mu m^2$
T	Temperature	300 K
n	a relative density of myosin motors	$24000\ \mu m^{-2}$
α	Coefficient for tension-driving myosin flow	1.6 μm
c_0	Initial myosin density	0.25
Γ	Line tension	30 nN
M	Mobility parameter of myosin motors	$1.9 \times \frac{10^5 \mu m^4}{s}/pJ$
L	Mobility parameter of focal adhesions	$1.5 \times \frac{10^3 \mu m^2}{s}/k_B T$

Tab. A.4. Model parameter used for patterned strip-shape cells.

Appendix B
Supplementary figures to determine the phase diagram on actin node formation

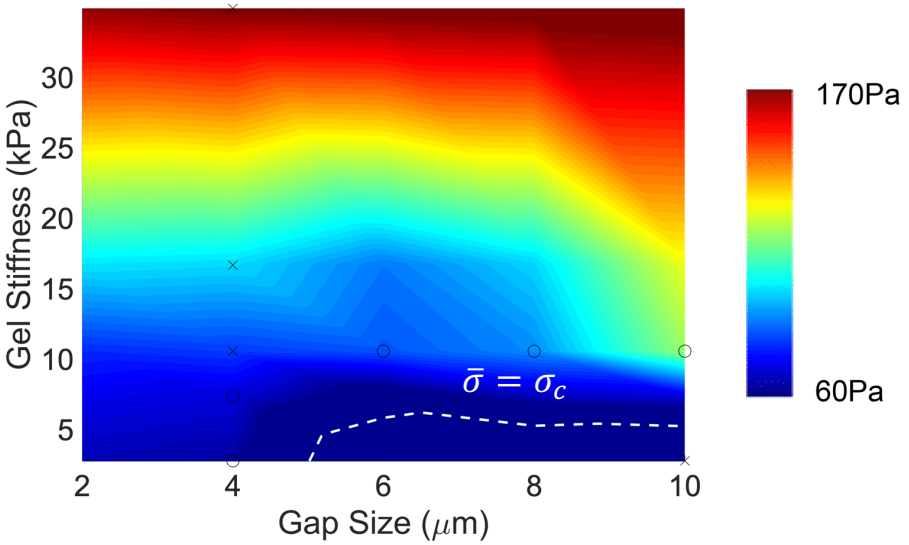

Fig. B.1. The phase diagram on $\bar{\sigma}$, overlapped with the action node formation of cells observed in the experiments. The horizontal axis is for the gap size, while the perpendicular axis is for the gel stiffness. A phase boundary of $\bar{\sigma} = \sigma_c = 70$Pa is identified by the white dashed line. The symbol "◯" stands for the success of actin node formation, while "×" stands for the failure of actin node formation.

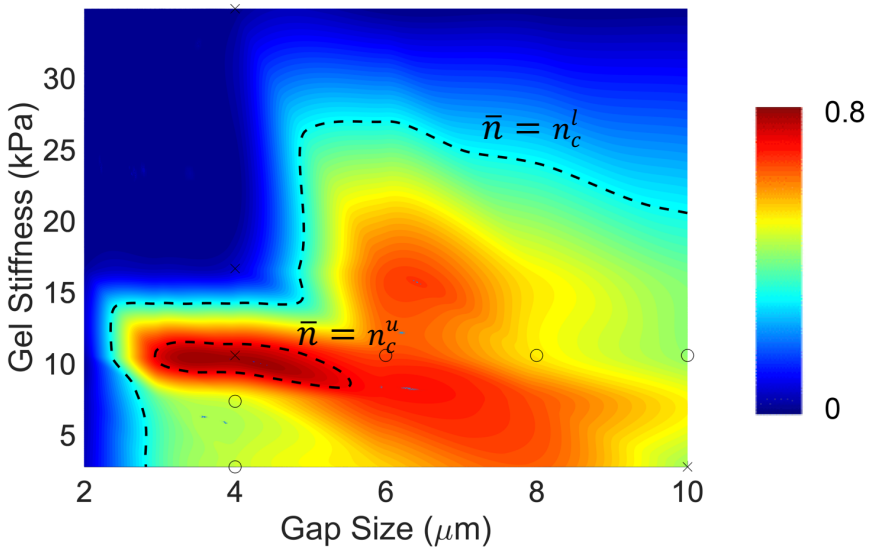

Fig. B.2. The phase diagram on $\bar{n}$, overlapped with the action node formation of cells observed in the experiments. The horizontal axis is for the gap size, while the perpendicular axis is for the gel stiffness. Two phase boundaries of $\bar{n} = n_c^u = 0.7$, and $\bar{n} = n_c^l = 0.3$, are identified by the black dashed lines. The symbol "◯" stands for the success of actin node formation, while "×" stands for the failure of actin node formation.

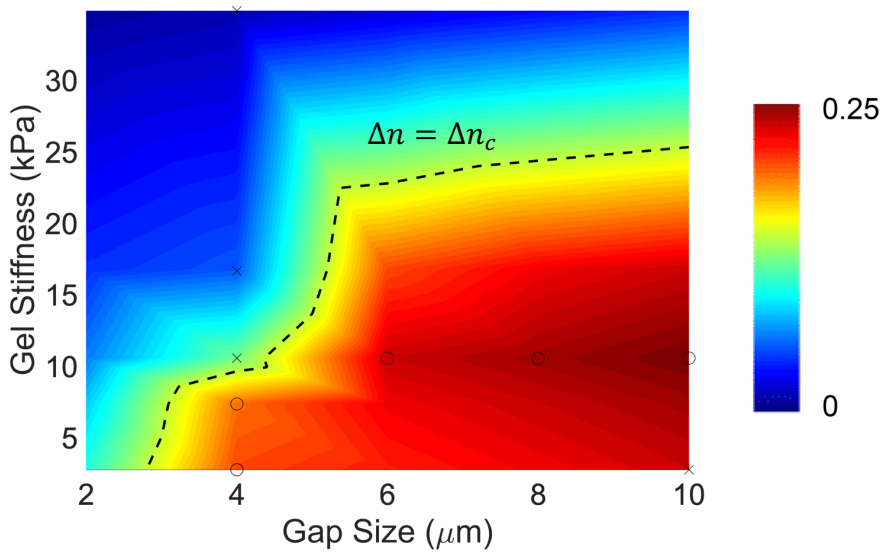

Fig. B.3. The phase diagram on Δn, overlapped with the action node formation of cells observed in the experiments. The horizontal axis is for the gap size, while the perpendicular axis is for the gel stiffness. The phase boundary of $\Delta n = \Delta n_c = 0.14$ is identified by the black dashed line. The symbol "◯" stands for the success of actin node formation, while "×" stands for the failure of actin node formation.

References

1. Wang, N., J.P. Butler, and D.E. Ingber, *Mechanotransduction across the cell surface and through the cytoskeleton.* Science, 1993 **260**(5111): p. 1124-1127.
2. Jaalouk, D.E. and J. Lammerding, *Mechanotransduction gone awry.* Nat Rev Mol Cell Biol, 2009, **10**(1): p. 63-73.
3. Huang, S. and D.E. Ingber, *Cell tension, matrix mechanics, and cancer development.* Cancer cell, 2005. **8**(3): p. 175-176.
4. DuFort, C.C., M.J. Paszek, and V.M. Weaver, *Balancing forces: architectural control of mechanotransduction.* Nature reviews: Molecular cell biology, 2011, **12**(5): p. 308-319.
5. Paszek, M.J., et al., *Tensional homeostasis and the malignant phenotype.* Cancer Cell, 2005, **8**(3): p. 241-254.
6. Zaidel-Bar, R., et al., *Hierarchical assembly of cell–matrix adhesion complexes.* Biochemical Society Transactions, 2004, **32**(3): p. 416-420.
7. Chen, C.S., J. Tan, and J. Tien, *Mechanotransduction at cell-matrix and cell-cell contacts.* Annu. Rev. Biomed. Eng., 2004, **6**: p. 275-302.
8. Balaban, N.Q., et al., *Force and focal adhesion assembly: a close relationship studied using elastic micropatterned substrates.* Nature cell biology, 2001, **3**(5): p. 466-472.
9. Riveline, D., et al., *Focal contacts as mechanosensors externally applied local mechanical force induces growth of focal contacts by an mdia1-dependent and rockindependent mechanism.* The Journal of cell biology, 2001, **153**(6): p. 1175-1186.
10. Vasioukhin, V. and E. Fuchs, *Actin dynamics and cell–cell adhesion in epithelia.* Current opinion in cell biology, 2001, **13**(1): p. 76-84.
11. Balda, M.S. and K. Matter, *Tight junctions.* Journal of Cell Science, 1998, **111**(5): p. 541-547.
12. Kumar, N.M. and N.B. Gilula, *The gap junction communication channel.* Cell, 1996, **84**(3): p. 381-388.
13. Wang, J.-C. and J.-S. Lin, *Cell traction force and measurement methods.* Biomechanics and Modeling in Mechanobiology, 2007, **6**(6): p. 361-371.
14. Landau, L.D., et al., *Theory of Elasticity: Vol. 7 of Course of Theoretical Physics*. Vol. 13. 1960: Physics Today. 44.
15. Yang, M.T., et al., *Assaying stem cell mechanobiology on microfabricated elastomeric substrates with geometrically modulated rigidity.* Nat. Protocols, 2011, **6**(2): p. 187-213.
16. Schwarz, U.S., et al., *Calculation of forces at focal adhesions from elastic substrate data: the effect of localized force and the need for regularization.* Biophysical journal, 2002, **83**(3): p. 1380-1394.
17. Sabass, B., et al., *High Resolution Traction Force Microscopy Based on Experimental and Computational Advances.* Biophysical Journal, 2008, **94**(1): p. 207-220.
18. Mertz, Aaron F., et al. *Scaling of traction forces with the size of cohesive cell colonies.* Physical review letters, 2012, 108.19: 198101.
19. Banerjee, Shiladitya, and M. Cristina Marchetti. *Contractile stresses in cohesive cell layers on finite-thickness substrates*. Physical review letters, 2012, 109.10: 108101.
20. Banerjee, Shiladitya, and M. Cristina Marchetti. *Controlling cell–matrix traction forces by extracellular geometry.* New Journal of Physics, 2013, 15.3: 035015.
21. Oakes, Patrick W., et al. *Geometry regulates traction stresses in adherent cells*. Biophysical journal, 2014, 107.4: 825-833.

22. Deshpande, Vikram S., Robert M. McMeeking, and Anthony G. Evans. *A bio-chemo-mechanical model for cell contractility*. Proceedings of the National Academy of Sciences, 2006, 103.38: 14015-14020.
23. Deshpande, Vikram S., et al. *A bio-mechanical model for coupling cell contractility with focal adhesion formation*. Journal of the Mechanics and Physics of Solids, 2008, 56.4: 1484-1510.
24. Shenoy, Vivek B., Hailong Wang, and Xiao Wang. *A chemo-mechanical free-energy-based approach to model durotaxis and extracellular stiffness-dependent contraction and polarization of cells.* Interface Focus, 2016, 6.1: 20150067.
25. Trepat, X., et al., *Physical forces during collective cell migration.* Nature Physics, 2009, 5(6): p. 426-430.
26. Crosby, L.M. and C.M. Waters, *Epithelial repair mechanisms in the lung.* American Journal of Physiology-Lung Cellular and Molecular Physiology, 2010, **298**(6): p. L715-L731.
27. Kuipers, D., et al., *Epithelial repair is a two-stage process driven first by dying cells and then by their neighbours.* Journal of cell science, 2014, **127**(6): p. 1229-1241.
28. Kim, J.H., et al., *Propulsion and navigation within the advancing monolayer sheet.* Nat. Mater, 2013, **12**(9): p. 856-863.
29. Vedula, S.R.K., et al., *Mechanics of epithelial closure over non-adherent environments.* Nature Communications, 2015, 6: 1-10.
30. Brugués, A., et al., *Forces driving epithelial wound healing.* Nature Physics, 2014, **10**(9): p. 683-690.
31. Ferrari, Mauro. *Cancer nanotechnology: opportunities and challenges*. Nature reviews cancer, 2005, 5.3: 161-171.
32. Peer D, Karp J M, Hong S, et al. *Nanocarriers as an emerging platform for cancer therapy*. Nature nanotechnology, 2007, 2(12): 751.
33. Burridge K, Chrzanowska-Wodnicka M. *Focal adhesions, contractility, and signaling*. Annual review of cell and developmental biology, 1996, 12(1): 463-519.
34. Huveneers S, Danen E H J. *Adhesion signaling–crosstalk between integrins, Src and Rho*. Journal of cell science, 2009, 122(8): 1059-1069.
35. Schwartz M A, DeSimone D W. *Cell adhesion receptors in mechanotransduction*. Current opinion in cell biology, 2008, 20(5): 551-556.
36. Puklin-Faucher E, Sheetz M P. *The mechanical integrin cycle*. Journal of cell science, 2009, 122(2): 179-186.
37. Goldmann W H. *Mechanotransduction and focal adhesions*. Cell biology international, 2012, 36(7): 649-652.
38. Sakamoto Y, Ogita H, Hirota T, et al. *Interaction of Integrin αvβ3 with Nectin IMPLICATION IN CROSS-TALK BETWEEN CELL-MATRIX AND CELL-CELL JUNCTIONS.* Journal of Biological Chemistry, 2006, 281(28): 19631-19644.
39. Siu M K Y, Cheng C Y. *Dynamic cross‐talk between cells and the extracellular matrix in the testis*. Bioessays, 2004, 26(9): 978-992.
40. Luo, Q., Kuang, D., Zhang, B. & Song, G. *Cell stiffness determined by atomic force microscopy and its correlation with cell motility.* Biochimica et Biophysica Acta (BBA)-General Subjects, 2016, 1860: 1953-1960.
41. Leckband D, Israelachvili J. *Intermolecular forces in biology*. Quarterly reviews of biophysics, 2001, 34(2): 105.

42. Bischofs, Ilka B., Sebastian S. Schmidt, and Ulrich S. Schwarz. *Effect of adhesion geometry and rigidity on cellular force distributions.* Physical review letters, 2009 103.4: 048101.
43. Discher, D.E., Janmey, P. & Wang, Y.L. *Tissue cells feel and respond to the stiffness of their substrate*. Science, 2005, 310: 1139-1143.
44. Tee, S.Y., Fu, J., Chen, C.S. & Janmey, P.A. *Cell shape and substrate rigidity both regulate cell stiffness*. Biophys. J., 2011, 100: L25-L27.
45. Trichet, L. et al. *Evidence of a large-scale mechanosensing mechanism for cellular adaptation to substrate stiffness*. Proceedings of the National Academy of Sciences, 2012, 109: 6933-6938.
46. Davis M E, Chen Z, Shin D M. *Nanoparticle therapeutics: an emerging treatment modality for cancer*. Nanoscience and technology: A collection of reviews from nature journals. 2010: 239-250.
47. Gao H, Shi W, *Freund L B. Mechanics of receptor-mediated endocytosis.* Proceedings of the National Academy of Sciences, 2005, 102(27): 9469-9474.
48. Zhang S, Gao H, Bao G. *Physical principles of nanoparticle cellular endocytosis*. ACS nano, 2015, 9(9): 8655-8671.
49. Yuan H, Li J, Bao G, et al. *Variable nanoparticle-cell adhesion strength regulates cellular uptake*. Physical review letters, 2010, 105(13): 138101.
50. Zhang S, Li J, Lykotrafitis G, et al. *Size-dependent endocytosis of nanoparticles*. Advanced materials, 2009, 21(4): 419-424.
51. Cross S E, Jin Y S, Rao J, et al. *Nanomechanical analysis of cells from cancer patients*. Nature nanotechnology, 2007, 2(12): 780-783.
52. Wei Q, Huang C, Zhang Y, et al. *Mechanotargeting: Mechanics-Dependent Cellular Uptake of Nanoparticles*. Advanced Materials, 2018, 30(27): 1707464.
53. Tambe, D.T. et al. *Collective cell guidance by cooperative intercellular forces*. Nat. Mater. 10, 469-475 (2011).
54. Tambe, D.T. et al. *Monolayer stress microscopy: Limitations, artifacts, and accuracy of recovered intercellular stresses*. PLoS One, 2013, 8: e55172.
55. Friedl P, Alexander S. *Cancer invasion and the microenvironment: plasticity and reciprocity.* Cell, 2011, 147(5): 992-1009.
56. Angelini T E, Hannezo E, Trepat X, et al. *Cell migration driven by cooperative substrate deformation patterns*. Physical review letters, 2010, 104(16): 168104.
57. Serra-Picamal X, Conte V, Vincent R, et al. *Mechanical waves during tissue expansion*. Nature Physics, 2012, 8(8): 628-634.
58. Zhang Y, Shi X, Zhao T, et al. *A traction force threshold signifies metastatic phenotypic change in multicellular epithelia*. Soft matter, 2019, 15(36): 7203-7210.
59. Deguchi S, Ohashi T, Sato M. *Tensile properties of single stress fibers isolated from cultured vascular smooth muscle cells*. Journal of biomechanics, 2006, 39(14): 2603-2610.
60. Luo Y, Xu X, Lele T, et al. *A multi-modular tensegrity model of an actin stress fiber*. Journal of biomechanics, 2008, 41(11): 2379-2387.
61. Tang X, Wen Q, Kuhlenschmidt T B, et al. *Attenuation of cell mechanosensitivity in colon cancer cells during in vitro metastasis*. PLoS One, 2012, 7(11).
62. Neufurth M, Wang X, Schröder H C, et al. *Engineering a morphogenetically active hydrogel for bioprinting of bioartificial tissue derived from human osteoblast-like SaOS-2 cells*. Biomaterials, 2014, 35(31): 8810-8819.

63. Tang X, Saif T. *Loss of cell adhesion in colon cancer cells during in vitro metastasis measured by bio-mems force sensor*. ASME 2012 Summer Bioengineering Conference. American Society of Mechanical Engineers Digital Collection, 2012: 251-252.
64. Saez A, Buguin A, Silberzan P, et al. *Is the mechanical activity of epithelial cells controlled by deformations or forces?*.Biophysical journal, 2005, 89(6): L52-L54.
65. Ghibaudo M, Saez A, Trichet L, et al. *Traction forces and rigidity sensing regulate cell functions*. Soft Matter, 2008, 4(9): 1836-1843.
66. Mitrossilis D, Fouchard J, Guiroy A, et al. *Single-cell response to stiffness exhibits muscle-like behavior*. Proceedings of the National Academy of Sciences, 2009, 106(43): 18243-18248.
67. Pellegrin SaM H. *Actin stress fibers*. Journal of cell science, 2007, 120: 3491-3499.
68. Sawada Y, Tamada M, Dubin-Thaler B J, et al. *Force sensing by mechanical extension of the Src family kinase substrate p130Cas*. Cell, 2006, 127(5): 1015-1026.
69. Katoh K, Kano Y, Amano M, et al. *Rho-kinase–mediated contraction of isolated stress fibers*. The Journal of cell biology, 2001, 153(3): 569-584.
70. Chen L Q. *Phase-field models for microstructure evolution*. Annual review of materials research, 2002, 32(1): 113-140.
71. Chen L, Fan F, Hong L, et al. *A phase-field model coupled with large elasto-plastic deformation: application to lithiated silicon electrodes*. Journal of The Electrochemical Society, 2014, 161(11): F3164-F3172.
72. Chen T, Callan-Jones A, Fedorov E, et al. *Large-scale curvature sensing by directional actin flow drives cellular migration mode switching*. Nature physics, 2019, 15(4): 393-402.
73. Mertz A F, Che Y, Banerjee S, et al. *Cadherin-based intercellular adhesions organize epithelial cell–matrix traction forces*. Proceedings of the National Academy of Sciences, 2013, 110(3): 842-847.
74. Liu Z, Tan J L, Cohen D M, et al. *Mechanical tugging force regulates the size of cell–cell junctions*. Proceedings of the National Academy of Sciences, 2010, 107(22): 9944-9949.
75. Borghi N, Sorokina M, Shcherbakova O G, et al. *E-cadherin is under constitutive actomyosin-generated tension that is increased at cell–cell contacts upon externally applied stretch*. Proceedings of the National Academy of Sciences, 2012, 109(31): 12568-12573.
76. Maruthamuthu V, Sabass B, Schwarz U S, et al. *Cell-ECM traction force modulates endogenous tension at cell–cell contacts*. Proceedings of the National Academy of Sciences, 2011, 108(12): 4708-4713.
77. Foty R A, Steinberg M S. *The differential adhesion hypothesis: a direct evaluation*. Developmental biology, 2005, 278(1): 255-263.
78. Ladoux B, Anon E, Lambert M, et al. *Strength dependence of cadherin-mediated adhesions*. Biophysical journal, 2010, 98(4): 534-542.
79. Borghi N, Lowndes M, Maruthamuthu V, et al. *Regulation of cell motile behavior by crosstalk between cadherin-and integrin-mediated adhesions*. Proceedings of the National Academy of Sciences, 2010, 107(30): 13324-13329.
80. Kleinfeld D, Kahler K H, Hockberger P E. *Controlled outgrowth of dissociated neurons on patterned substrates*. Journal of Neuroscience, 1988, 8(11): 4098-4120.
81. Matsuzawa M, Potember R S, Krauthamer V. *Use of chemically patterned substrate to study directional effect of damaging electrical stimulation on cultured neuroblastoma cells*. Brain research, 1994, 667(1): 47-53.

82. Thomas C H, McFarland C D, Jenkins M L, et al. *The role of vitronectin in the attachment and spatial distribution of bone-derived cells on materials with patterned surface chemistry*. Journal of Biomedical Materials Research: An Official Journal of The Society for Biomaterials and The Japanese Society for Biomaterials, 1997, 37(1): 81-93.
83. Detrait E, Lhoest J B, Knoops B, et al. *Orientation of cell adhesion and growth on patterned heterogeneous polystyrene surface*. Journal of neuroscience methods, 1998, 84(1-2): 193-204.
84. Torimitsu K, Kawana A. *Selective growth of sensory nerve fibers on metal oxide pattern in culture*. Developmental Brain Research, 1990, 51(1): 128-131.
85. Valentini R F, Vargo T G, Gardella J A, et al. *Patterned neuronal attachment and outgrowth on surface modified, electrically charged fluoropolymer substrates*. Journal of Biomaterials Science, Polymer Edition, 1994, 5(1-2): 13-36.

Curriculum Vitae

Tiankai Zhao

EDUCATION：

2015- **PhD Candidate in Engineering Sciences and Mechanics**

Pennsylvania State University, supervised by Dr. Sulin Zhang

2013-2014 **Master of Sci. in Mechanics, Materials and Computing**

Carnegie Mellon University, supervised by Dr. Amit Acharya

2009-2013 **Bachelor of Engr. in Engineering Mechanics**

Huazhong University of Science and Technology, Wuhan, Hubei Province, China

JOURNAL PUBLICATIONS:

1. **Zhao, T**., Zhang, Y., Wei, Q., Shi, X., Zhao, P., Chen, L. Q., & Zhang, S. (2018). Active cell-matrix coupling regulates cellular force landscapes of cohesive epithelial monolayers. *Npj Computational Materials*, *4*(1), 10.
2. Wei, Q., Huang, C., Zhang, Y., Zhao, **T., Zhao**, P., Butler, P., & Zhang, S. (2018). Mechanotargeting: Mechanics-Dependent Cellular Uptake of Nanoparticles. *Advanced Materials*, *30*(27), 1707464.
3. Zhang, G., Zhao, P., Zhang, X., Han, K., **Zhao, T.**, Zhang, Y., ... & Wang, Q. (2018). Flexible three-dimensional interconnected piezoelectric ceramic foam-based composites for highly efficient concurrent mechanical and thermal energy harvesting. *Energy & Environmental Science*, *11*(8), 2046- 2056.
4. Zhang, Y., Shi, X., **Zhao, T.**, Huang, C., Wei, Q., Tang, X., ... & Zhang, S. (2019). A traction force threshold signifies metastatic phenotypic change in multicellular epithelia. *Soft matter*, *15*(36), 7203- 7210.
5. Zhang Y, Wei Q, Zhao T, et al. (2019) Extracellular and intercellular force distribution in circularly shaped epithelia. *Extreme Mechanics Letters, 31*: 100526.
6. **Zhao, T.**, Zhu, J., & Luo, J. (2016). Study of crack propagation behavior in single crystalline tetragonal zirconia with the phase field method. *Engineering Fracture Mechanics*, *159*, 155 173.
7. **Zhao, T.**, Luo, J., & Xiao, Z. (2015). Buckling analysis of a nanowire lying on Winkler–Pasternak elastic foundation. *Mechanics of Advanced Materials and Structures*, *22*(5), 394-401.